Unveiling $BiVO_4$ Nanorods as a Novel Anode Material for High Performance Lithium Ion Capacitor: Beyond intercalation strategy

*Deepak P. Dubal,[a, b]** Kolleboyina Jayaramulu,[c,d] Radek Zboril,[d] Roland A. Fischer,[c] Pedro Gomez-Romero [b]**

[a]Dr. D. P. Dubal
School of Chemical Engineering, The University of Adelaide, Adelaide, South Australia 5005, Australia
E-mail: dubaldeepak2@gmail.com

[b]Dr. D. P. Dubal, Prof. Dr. P. Gomez-Romero
Catalan Institute of Nanoscience and Nanotechnology (ICN2), CSIC and the Barcelona Institute of Science and Technology, Campus UAB, Bellaterra 08193, Barcelona, Spain
Email: pedro.gomez@icn2.cat

[c]Dr. K. Jayaramulu, Prof. Dr. R. A. Fischer
Chair of Inorganic and Metal-Organic Chemistry, Department of Chemistry and Catalysis Research Centre, Technical University of Munich, 85747 Garching, Germany

[d]Dr. K. Jayaramulu, Prof. Dr. R. Zboril
Regional Centre of Advanced Technologies and Materials, Faculty of Science, Palacky University, Šlechtitelů 27, 783 71, Olomouc, Czech Republic

Keywords: Li-ion capacitors, metal vanadates, partially reduced graphene oxide (PRGO), Energy Storage, Energy Density.

Abstract

Energy storage is increasingly demanded in many new niches of applications from wearables to unmanned autonomous vehicles. However, current energy storage systems are unable to fulfill the power requirements (high energy at high power) needed for these novel applications. Recently, Li-ion capacitors (LICs) have been spotted as hybrid device with the potential to display high energy and high power. Nevertheless, it is still a great challenge to achieve high performance LICs due to the unmatched kinetic property and capacity between anode and cathode materials. Herein, we are presenting our first seminal report on the use of $BiVO_4$ nanorods as a new anode material for LICs coupled with a partially reduced graphene oxide (PRGO) cathode. The $BiVO_4$ nanorods show an excellent reversible capacity of 877 mAh/g (ultrahigh volumetric capacity of 4560 mAh/cm^3) at 1.1 A/g with a great capacity retention (in half-cell design), which is highest value reported so far for metal vanadates. Later on, a LIC was constructed with $BiVO_4$ as an anode and PRGO as a cathode electrode delivering high energy density of 152 Wh/kg and a maximum power density of 9.6 kW/kg compared to that for hard carbon and intercalation (such as $Li_4Ti_5O_{12}$, Li_3VO_4) based anode materials. Additionally, $BiVO_4$//PRGO LIC exhibits good cyclability of 81 % over 6000 cycles. Thus, this investigation opens up new opportunities to develop different LIC systems.

1. Introduction

The energy landscape is quickly changing, especially concerning the generation of electricity, and energy storage is in great demand from new niche and mainstream sectors, from wearable electronics to electric vehicles. Thus, very harsh new requirements are now expected from batteries, including low cost and extended cyclability added to high energy and high power densities. This combination is hard to achieve for conventional energy storage systems such as Li-batteries (LIB) and Supercapacitors.[1-3] A Lithium Ion Capacitor (LIC) is precisely the type of hybrid device which could power our future due to its excellent energy and power densities. [4, 5] Generally, LICs are fabricated with a battery electrode (commonly the anode) and a supercapacitor double-layer cathode with a Li-salt based organic electrolyte, [6-8] leading to enhanced energy and power densities. [9]

The final performance of LIC is strongly depends on the cathode and anode materials as well as their device combination. Concerning cathode materials for LICs, activated carbon (AC) constitutes the most frequently used and effective material due to useful characteristics such as electronic conductivity, excellent surface area and cost-effectiveness.[10, 11] However, their low capacity is still limiting the overall electrochemical performance of LIC devices. Conversely, several materials have been investigated as promising anodes for LICs such as $Li_4Ti_5O_{12}$ [6, 12, 13] TiP_2O_7 [14] TiO_2-B, [15] $LiCrTiO_4$ [16] etc. Among these materials, $Li_4Ti_5O_{12}$ made a great contribution to the field due to its remarkable structural properties such as good reversibility, reasonable capacity, negligible volume changes during lithium insertion/extraction as well as low cost and excellent cycle life.[6, 12, 13] Unfortunately, its limited energy density (34 Wh/kg) when combined with AC due to the low amount of lithium uptake (theoretical capacity of ~175 mAh/g) hampers their application in LICs. [17] Therefore, to achieve adequate energy density and power to drive electric vehicles (HEVs and EVs) a suitable anode and cathode materials with high capacity and good reversibility needs to be coupled together. Thus, the design and combination of ideal cathode and anode materials to realise best LIC performance is still a challenge.

Recently, Vanadium-based materials are attracting much attention as Li-ion electrodes due to their multivalence states and the rich inorganic chemistry of many different metal vanadates such as Li_3VO_4, $FeVO_4$, $BiVO_4$, ZnV_2O_4 and NiV_3O_8.[18-21] Among them, Li_3VO_4 has been extensively investigated due to

its excellent electrochemical properties such as high capacity (323 mAh/g) and good reversibility.[22-24] In addition, $FeVO_4$ has been studied lately as a promising LIB anode material with theoretical capacity of 847 mAh/g (5.4 mol Li per $FeVO_4$). [19] For instance, Yan et al [25], applied $FeVO_4$ nanorods in LIB and achieved a reversible discharge capacity of 527 mAh/g at 75 mA/g current rate (see Table S1).

Here, we are introducing a new vanadate i.e. Bismuth Vanadate ($BiVO_4$) as a promising electrode for ultrahigh volumetric capacity LIBs. Typically, $BiVO_4$ has been presented as a most successful material in the field of photocatalysis. In our previous reports, we applied $BiVO_4$ in high energy density supercapacitors. [26, 27] Herein, for the first time, we have employed $BiVO_4$ as an anode material in LICs. The motivation to use this material in LIBs is its unique layered crystal structure as well as the integration of multivalent Bi and V elements where Bi is well known anode based on Bi-Li alloying mechanism. [28] In the last century, there was the first and only report on $BiVO_4$ used as a cathode in a primary lithium cell. [29] Furthermore, to construct truly high-performance LICs one needs to pair suitable capacitor-type and battery-type electrodes in a kinetically balanced device where quick surface polarization by the double-layer capacitive electrode must be balanced with the much slower electro-ionic process of the battery electrode, which is a great challenge.

In present investigation, we have designed and assembled a lithium ion capacitor (LIC) based on $BiVO_4$ nanorods as anode (battery-type) coupled with partially reduced graphene oxide (PRGO) as cathode (capacitor-type) materials. The use of PRGO cathode allows swift surface reactions associated to a substantial enhancement of Li storage capacity due to the presence of surface functional groups.[30, 31] In brief, $BiVO_4$ nanorods were prepared by hydrothermal route whereas PRGO nanosheets were prepared with Hummers method. The electrochemical properties of $BiVO_4$ and PRGO were firstly tested in half-cell configuration (vs Li-metal). The detailed Li storing mechanism of $BiVO_4$ was studied. Finally, the LIC was fabricated with $BiVO_4$ nanorods and PRGO electrodes by balancing the mass of the electrodes and its electrochemical performance was investigated.

2. Results and Discussion

2.1. Characterizations of $BiVO_4$ Nanorods

The XRD pattern with Rietveld-refinement presented in Figure 1 (a) confirms the formation of phase-pure monoclinic $BiVO_4$ (*C*2/*c* space group) [JCPDS: 014-0688]. The initial structural parameters were taken from the earlier report. [32] The lattice parameters obtained from the refinement are a = 7.2558 Å, b = 11.7091 Å, c = 5.0964 Å and β = 134.24º which are consistent with the literature results. [33] From the crystal structure, it is seen that the unit cell of $BiVO_4$ is composed of BiO_8 dodecahedron and VO_4 tetrahedron where the similar metal atoms are connected to each other in continuous zigzag manner with distances about 3.85 Å. Moreover, since the Bi and V atoms are alternately arranged along the crystallographic 'c' axis, $BiVO_4$ exhibits the characteristics of layered structure (see Figure 1b) which can be feasible for Li ion storage. Further, the oxidation states of Bi and V in $BiVO_4$ were investigated by XPS analyses and presented in Figure 1 (c-d). The magnified Bi4f spectrum shows two peaks at binding energies of 159.3 eV and 164.5 eV, suggesting that Bi is in 3+ oxidation state (Figure 1c). The $Bi4f_{5/2}$ and $Bi4f_{7/2}$ peaks are well resolved with spin orbit splitting of 5.32 eV. Similarly, the V2p spectrum exhibits two peaks at binding energies of 516.9 eV ($V2p_{3/2}$) and 524.4 eV ($V2p_{1/2}$), indicating that V is in +5 oxidation state. [27, 34] The XPS spectrum of O1s is fitted in two components at binding energies of 530.1 eV and 532.1 eV which are attributed to metal oxygen and surface hydroxyl oxygen, respectively [27] (see Figure S1).

An interesting and innovative morphological feature is obtained for $BiVO_4$ sample as displayed in Figure 2. It is revealed that the $BiVO_4$ exhibits a cluster of banana blossoms-like nanostructure (Figure 2 a, b). The size and shapes of all these blossoms are uniform suggesting the controlled hydrothermal growth of the nanostructure (Figure S2). The blossoms have sharp tips at both ends and the size of nanorods is around 800-850 nm in length and around 90-95 nm in diameters (Figure 2c). High-magnified TEM image further implies the formation of nanorods (see Figure 2d), suggesting the size of around 40 nm (Figure S3). Figure 2 (e) shows the inverse fast Fourier Transform (FFT) image of the selected area shown by white rectangle in Figure 2d. The interplaner spacing was found to be 0.467 nm which

corresponds to (011) plane of monoclinic $BiVO_4$. Additionally, SAED pattern made the final approval of formation of monoclinic $BiVO_4$ structure as shown in Figure 2 (f).

2.2 Li-ion battery performance of $BiVO_4$ Anode

To begin with, $BiVO_4$ nanorods electrode was tested in half-cell configuration with Li-metal as both counter and reference electrode. The brief electrochemical insights are provided by cyclic voltammetry measurements as shown in Figure 3 (a). The CV curves strongly resembles to two materials Bi-based anode and Li_3VO_4 electrode.[35, 36] There were four reduction peaks observed in the first CV cycle at about 1.96 V, 1.65 V, 0.89 V and 0.51 V. The first peak at 1.96 V can be assigned to the decomposition of the electrolyte and the formation of the solid electrolyte interface (SEI) [37] while the peaks at 1.65 V and 0.89 V might be associated to the formation of metallic Bi and reduction of V^{5+} (V^{5+} to V^{4+}), respectively. In case of cathodic peak at 0.51 V, there are two possibilities, one is reduction of V^{4+} to V^{3+} and other might be due to the reaction between Li and Bi to form Li_3Bi. [35, 36] Interestingly, in the subsequent cycle, this peak (0.51 V) split into two peaks around 0.48 V and 0.7 V which are attributed to the reduction of V^{4+} to V^{3+} and formation of Li_3Bi, respectively. [36, 38] In the first anodic cycle, three oxidation peaks at about 0.97 V, 1.4 V and 2.72 V are clearly observed. Among which, the peaks at 0.97 V and 1.4 V are attributed to the de-alloying of Bi and oxidation of V^{3+} to V^{5+}, respectively while the anodic peak at 2.72 corresponds to the oxidation of metallic Bi. It is not surprising that the peaks at 1.65 V in cathodic and 2.72 V in anodic scan disappeared in the couple of subsequent cycles due to their irreversible nature. However, it should be noted that the redox peaks corresponding to Bi alloying/dealloying (cathodic 0.7 V/ anodic 0.97 V) as well as redox transitions of V (0.89 V, 0.48 V, cathodic and 1.37-1.64 V, anodic) are extremely reversible for the next cycles. [36-38] Thus, this unique material can provide properties of two charge storage mechanisms such as alloying/dealloying as well as faradaic redox transitions and expected to provide high capacity.

The galvanostatic charge/discharge (GCD) curves further show similar trends like CV measurements. Figure 3 (b) shows first ten GCD curves of $BiVO_4$ electrodes in half cell configuration measured at 0.06 A/g. The initial discharge and charge capacities are found to be 1730 mAh/g and 1177 mAh/g with Coulombic efficiency of 67 %. In the subsequent cycle, a discharge capacity was 1296

mAh/g which keeps decreasing for next few cycles and obtained a stable discharge capacity of 877 mAh/g after 7th cycle, suggesting comparable or even better performance than other vanadates (see Table S1). [39-43] The decrease in the capacity during initial few cycles may corresponds to SEI formation and conversion of electrode materials into stable phase. It is also interesting that after first discharge/charge cycle the Coulombic efficiency is maintained at around 100 %. The theoretical capacity calculated to be 662 mAh/g, which is not sufficient to explain the higher capacity of $BiVO_4$ obtained experimentally (877 mAh/g). It is reported that, the anion (i.e., oxygen) plays a crucial role during the lithium reaction where it can act as a redox center leading to possible Bi-"O-Li" and V-"O-Li" interactions (Figure S4).[19] This can result in an enhancement in the specific capacity. Furthermore, this discharge capacity can be translated to the excellent volumetric capacity of 4560 mAh/cm^3, considering the high bulk density of 5.2 gm/cm^3. The initial decrease in discharge capacity can be attributed to the activation of electrode material as well as decomposition of electrolyte and formation of a solid electrolyte interface (SEI) on the electrode. [37]

The rate capability of $BiVO_4$ nanorods at different current densities from 0.06 A/g to 11.45 A/g was investigated (Figure S5). Notably, the $BiVO_4$ nanorods show excellent Li-ion storing capability and cycling stability even at high rates. The reversible capacities are calculated to be 1035 mAh/g (5392 mAh/cm^3) and 326 mAh/g (1695 mAh/cm^3) at 0.12 and 11.45 A/g, respectively (Figure 3 c). It should be underscored that the $BiVO_4$ exhibits a reversible capacity of 326 mAh/g even at the high current density of 11.45 A/g, which is still a very substantial value (about 87 % of the theoretical capacity of graphite). Moreover, after changing the current density to 1.1 A/g after 80 cycles at various current densities, the $BiVO_4$ nanorods achieve a capacity of 793 mAh/g, signifying excellent rate capability. The cycling performance of $BiVO_4$ nanorods was investigated at 1.1 A/g over 500 cycles and is displayed in Figure 3 (d). They present an extraordinary cycling stability during charge/discharge with a negligible capacity loss after 500 cycles. The Coulombic efficiency of $BiVO_4$ electrodes is maintained above 80 % in the beginning and stabilized at 98 % over 500 cycles. This exceptional long-term stability may be ascribed to the unique nanorods like morphology which acts as buffering a volume expansion during charging/discharging and alloying/dealloying mechanism that maintains the high capacity for long cycling.

The Li-ion charge kinetics was further analyzed by estimating the capacitive and diffusion controlled charge contributions to the total charges stored by $BiVO_4$ electrode. [44] For this analysis, the CV curves were measured at different scan rates for $BiVO_4$ electrodes (in half-cell design) and presented in Figure S6. The slope of the corresponding log(ν) vs log(i) plot is $b = 0.66$ for cathodic peak and is consistent with kinetics dominated by diffusion-controlled process (Figure S5). The total charge stored in the $BiVO_4$ electrode is the sum of surface capacitive charge (Q_c) and diffusion-controlled charge (Q_d) which can be expressed as follows,

$$Q_t = Q_c + Q_d \quad (1)$$

The capacitive contribution (Q_c) is associated with the charges stored at the electrode/electrolyte interface (surface adsorption as well as surface redox reactions) and hence are scan rate independent. On the other hand, semi-infinite linear diffusion is assumed for the diffusion processes and thus, Q_d varies as the reciprocal square root of scan rate, hence the equation (2) can be rewritten as,

$$Q_t = Q_c + k\nu^{-1/2} \quad (2)$$

Where, k is a constant and Q_c can be determined by plotting Q_t against the reciprocal of the square root of scan rate ($\nu^{-1/2}$) (Figure S6). Figure 3 (e) shows the percent contribution of capacitive charge at different scan rates. The analysis suggests that about 62 % of total charge stored by $BiVO_4$ electrode is contributed from diffusion-controlled processes at 1 mV/s. Moreover, it is interesting that at a high scan rate of 5 mV/s, the capacitive and diffusion charge contributions are almost equal i. e. 49% and 51%, respectively, while at high scan rate of 10 mV/s, the capacitive charge is 78% due to the faster charge kinetics. Thus, the significant diffusion controlled charge contribution is attributed to the conversion reactions during the Li-interaction. The Li-ion diffusion coefficient in $BiVO_4$ electrode was further estimated by the Randles-Sevick equation: [41]

$$i_p = 2.69\times10^5 n^{3/2} A D_{Li}^{1/2} \nu^{1/2} C \quad (3)$$

where i_p is current maximum in amps (we considered current value at 3 points), n is number of electrons involved in the charge storage, A is electrode area in cm^2 (for simplicity we have considered

geometrical area), D_{Li} is diffusion coefficient in cm^2/s, ν is scan rate in V/s, C is concentration of Li-ion in mol/cm^3. The diffusion coefficients for $BiVO_4$ calculated at different peak currents is in the range of 10^{-9} cm^2/s for different scan rates (Figure 3f) which are greater than the values reported for other vanadates. [40, 41, 45] The diffusion coefficients for $BiVO_4$ increase with increasing scan rate, further confirming the high rate capability of the material. To further reveal the reasons for excellent Li-ion storage properties, the EIS measurements were carried out and shown in Fig. S7. The Nyquist plots for $BiVO_4$ tested at different discharging and charging potentials exhibit a depressed semicircle in the high- and middle-frequency regimes and a straight line in the low-frequency region. The straight-line region corresponds to the semi-infinite diffusion of Li ions while the depressed semicircle can be assigned to SEI film and contact resistance at high frequencies, and a charge-transfer process in the mid-frequencies, respectively. It is further noticed that the diameter of the semicircle increases slightly with the intercalaction of lithium ion, indicating that the film and contact resistances increase steadily which further decreases upon de-intercalation suggesting good reversibility. This suggests that the large Li capacity of $BiVO_4$ is due to the actual ion insertion/extraction process in the nanorods.

The detailed investigation of changes in the crystal structure of $BiVO_4$ was carried out by *Ex-situ* XRD analyses at different discharge/charge potentials and the results are presented in the Figure 4 (a, b). During the first discharge, *Ex-situ* XRD pattern measured at 1.2 V manifests the transformation of pure monoclinic $BiVO_4$ structure into completely new low crystalline material with some fresh peaks around 21.2º and 36.3º (marked with green stars) (see Figure 4a). These two new peaks correspond to the Li_3VO_4 phase [JCPDS No. 38-1247].[22] As the lithiation process reached to the end of discharge at 0.01 V, the slope region is observed due to SEI and the *Ex-situ* XRD reveals the appearance peaks related to Li_3Bi (alloying, marked with pink balls) [29, 46] with few weak peaks corresponding to the Li_3VO_4 .[22] In the next step, the *Ex-situ* XRD measured at 1.8 V show that the peaks related to both Li_3Bi and Li_3VO_4 loses their intensities confirming the dealloing and Li-extraction processes, respectively. At the complete charge state (3.5 V), it is seen that all the peaks disappeared and amorphous materials are formed which maintained their amorphous nature for subsequent cycles with some signatures of LiBi alloying and

Li_3VO_4 phase (Figure 4b). Thus, *Ex-situ* XRD analysis clearly resembles with CV and CD results explained in previous section.

More insights about the change in oxidation states of Bi and V during discharging/charging are investigated by *Ex-situ* XPS analyses. Figure 4 (c, d) shows the magnified spectra of Bi4f at different stages of electrode such as fresh, after first discharge and first charge. Interestingly, after first discharge the Bi4f peaks are completely shifted to the lower binding energies compared to the fresh electrodes. This may be assigned to the interaction between Bi and Li upon lithiation. The binding energies corresponding to $Bi4f_{7/2}$ and $Bi4f_{5/2}$ are found to be 156.8 eV and 162.1 eV with spin orbit splitting of 5.3 eV, perfectly matching to metallic Bi (Bi^0). Upon complete charging metallic Bi (Bi^0) returns to the original Bi^{3+} state suggesting excellent reversibility. Similarly, core-level XPS spectra of V2p suggests the transition of V^{5+} to V^{3+} and then from V^{3+} to V^{5+} upon discharging and charging. Note that, the vanadium is not fully recovered to +5 as seen in Figure 4 (d) which has already been observed in case of $FeVO_4$ electrode. [19]

These encouraging results demonstrate that, $BiVO_4$ can be promising anode material for Li-ion battery. To further show the practical applicability of this material, Li-ion capacitor has been assembled by using partially reduced graphene oxide (PRGO) as cathode material. The next section describes the electrochemical properties of PRGO in half-cell configuration.

2.3. Li-ion performance evaluation of PRGO cathode

We have used partially reduced graphene oxide (PRGO) cathodes as the counterpart to $BiVO_4$ anodes. First of all, graphene oxide (GO) was prepared by a modified Hummers method as described in the experimental section. In order to prepare partially reduced GO (PRGO), graphene oxide was annealed at 120 °C for 6 hr in air. The PRGO cathode was firstly characterized by XPS analysis in order to determine the content of oxygen. The C1s spectrum was fitted with three peaks centered at 284.6, 286.2 and 287.7 eV, corresponding to C-C, C-O and C=O, respectively, confirming the presence of considerable amounts of oxygen (Figure S8). Furthermore, the O1s peak could be fitted so that the peak entails primarily carbonyl groups (C=O) at 531.2 eV, and C-O at 533.4 eV as seen from Figure S7. The content of oxygen was calculated by the area ratio of O peak and the sum of C and O peaks (O/(C+O)).

The oxygen content was found to be around 33.8 % confirming the formation of partially reduced (leaving some oxygen functional groups) graphene oxide (PRGO) cathode.

In addition to the functional groups, an optimal electrode material should exhibit a porous microstructure for high electrochemical performance, since open-porosity enables greater permeation of the electrolyte ions into the bulk of the electroactive materials. Figure 5 (a) shows FESEM image of PRGO cathode. Interestingly, PRGO exhibits three dimensional (3D) networks of open-porous interconnected nanosheets (see Figure S9). The formation of open-porosity in PRGO is attributed to the fast gas release under the high vapor pressure produced due to the concentrated HCl treatment. The BET surface area and pore-size distributions measurements of PRGO sample were further investigated and shown in Figure S8. The specific surface area was found to be 214 m^2/g and exhibits most of the pores in meso/macroporous regime which can provide "super highways" for the electrolyte ions within the porous network and shorten the diffusion length.

The PRGO cathode was initially tested in a Li half-cell design between 1.5-4.5 V vs. Li/Li^+ and is displayed in Figure 5 (b-d). The nearly rectangular CV curves with small humps are observed for PRGO cathode at all the scan rates, indicating major contribution from EDLC and pseudo-capacitance (Figure S10a). This pseudo-capacitance must be ascribed to the presence of enormous oxygen functional groups on PRGO nanosheets. By fitting a log(current) vs log(scan rate) plot (Figure S10b), a '*b*' -value of 0.974 can be obtained, which indicates that a surface-controlled capacitive electrode process dominates the PRGO nanoheest cathode. Figure 5 (b) shows galvanostatic charge-discharge (GCD) curves of PRGO at different current densities from 0.1 A/g to 22 A/g. The linear and symmetric nature of these GCD profiles further confirms the capacitive behavior of this electrode material through adsorption/desorption of ions. Impressively, the PRGO cathode shows a maximum capacity of 145 mAh/g (~174 F/g) at 0.1 A/g which is considerably higher than that of activated carbon or other carbon-based cathodes. [47-50] Moreover, the PRGO cathode still delivers a capacity of 79.7 mAh/g (94 F/g) at very high current density of 22 A/g, suggesting excellent rate capabilities (see Figure 5 c). This excellent performance of PRGO might be attributed to the partial reduction of graphene oxide which increases electrical conductivity while maintaining a substantial amount of C=O redox groups. It is further interesting to note that, the

PRGO cathode exhibits excellent cycling stability with 92 % capacity retention over 4000 CD cycles at current density of 0.4 A/g. The slight humps (increase in capacity) are observed at around 2000, 2300 and 3200 cycles, which likely because of the gradual activation of functional groups within the PRGO electrode.[50] In addition, the Coulombic efficiency of PRGO increases from 90% to almost 100 % after 800 cycles and maintained there for next 4000 cycles as shown in Figure 5 (d). Thanks to the pseudo-capacitive redox reactions of functional groups (C=O/C–O)PRGO with the consequent Li^+ uptake which offers high charge storage capabilities in PRGO cathode. Moreover, this faradaic component has no detrimental effect on cycling because the reactions involved are molecular redox processes and do not involve phase transitions or volume change during charge/discharge.

Taking into account all these excellent electrochemical properties of PRGO in $LiPF_6$ electrolyte and its complementary electrochemical voltage, PRGO was expected to be a suitable cathode electrode to be combined with $BiVO_4$ anode in a LIC.

2.4. Full cell of $BiVO_4$//PRGO Li-ion capacitor (LIC)

Half-cell electrochemical testing confirm that $BiVO_4$ and PRGO electrodes operate reversibly in different and complementary potential windows (0.01 to 3.5 V and 1.5 V to 4.5 V, respectively (vs Li/Li^+) with different electrochemical mechanisms. This complementarity should naturally lead to an extended working voltage window. Before fabricating full LIC cell, both $BiVO_4$ and PRGO electrodes were pre-activated for 10 cycles at 0.2 A/g in Li-half cells. Note that, $BiVO_4$ electrode was fully charged (lithiated) up to 0.01 V (vs. Li) to allow for optimal working of the final device. The mass ratio of $BiVO_4$ to PRGO was calculated by balancing charges in cathode and anode and is maintained to be 1:5 (1.6 mg of $BiVO_4$ and 7.9 mg of PRGO). The electrochemical performances of $BiVO_4$//PRGO LIC cell were measured within the voltage range of 0.01-4.0 V. Figure 6 (a) shows GCD curves at different current densities from 0.46 A/g to 4.63 A/g. It is noted that the shapes of GCD curves exhibit the signatures of combined charge storing mechanisms involved in $BiVO_4$//PRGO LIC cell. Figure 6 (b) shows a charge/discharge curve for $BiVO_4$//PRGO LIC cell at 0.9 A/g with the corresponding potential profiles measured for cathode and anode (red and green curves, respectively). As expected, the anode and cathode electrodes work in the voltage ranges: 0.01 V to 2.25 V and 2.25 V to 4.0 V (vs Li/Li^+). In order to

investigate the rate capability of $BiVO_4$//PRGO device, the specific capacitances at different current densities with cycle number are calculated and plotted in Figure 6 (c). The specific capacitances for LIC cell were found to be 101 F/g and 22 F/g at 0.46 A/g and 11.6 A/g, respectively which was further maintained to 96 F/g when the current density is changed back to 0.46 A/g after 90 cycles signifying excellent rate capability of $BiVO_4$//PRGO cell. The variations of specific capacitance and specific capacity with current densities are shown in Figure 6 (d). The capacity was found to be 140 mAh/g, considering the mass of cathode material which suggests almost 98% utilization of PRGO cathode (by comparison with half-cell). The total capacity was calculated to be 114 mAh/g, considering total weight of active materials in both electrodes.

The Ragone plot for $BiVO_4$//PRGO LIC cell is shown in Figure 6 (e). On the high-energy corner of the ring, our system can deliver excellent energy density of 152 Wh/kg at a power density of 384 W/kg which is better than the reported LIC (see Supporting Information Table 2). On the high power corner, the $BiVO_4$//PRGO LIC can still deliver an energy density of 42 Wh/kg at 3861 W/kg, a combination that surpasses most supercapacitors in terms of energy density. The power and energy of this $BiVO_4$//PRGO LIC are even competitive with the best performing LICs energy storage devices reported, [15, 51-57] which have triggered considerable recent interest in the literature. A long cycling test was carried out at 0.9 A/g for 6000 charge/discharge cycles and results are shown in Figure 6 (f). It is worth noting that the LIC cell retains 81 % of its initial capacity after 6000 cycles, thereby confirming excellent reversibility and cycle life. Moreover, $BiVO_4$//PRGO LIC cell exhibits outstanding Coulombic efficiency of around 98 % over 6000 cycles. The $BiVO_4$ and PRGO samples were further characterized after 6000 cycles and results are presented in S.I. S10. It is revealed that both the samples preserves their amorphous nature and nanostructures after 6000 cycles, suggesting the potential candidates for high performance LICs (see Figure S11).

3. Conclusions

In summary, a high performance LIC based on $BiVO_4$ nanorods as anode and PRGO nanosheets as cathode was designed and implemented. In this first report, the $BiVO_4$ nanorods showed an excellent reversible capacity of 877 mAh/g (ultrahigh volumetric capacity of 4560 mAh/cm^3) with negligible

capacity loss over 500 cycles. Furthermore, 3D interconnected porous PRGO nanosheets showed high specific capacitance of 174 F/g (144 mAh/g) and excellent stability with 93 % capacity retention over 4000 cycles at Coulombic efficiency of 100 %. Later, a LIC cell based on $BiVO_4$ as an anode and PRGO as a cathode electrode delivers an exceptional energy density of 152 Wh/kg and a maximum power density of 9.6 kW/kg. This significant performance is attributed to unique $BiVO_4$ nanorods and which provides dual charge storing behavior (alloying and faradaic) and a 3D open-porous, interconnected PRGO nanosheet that provides short ion diffusion paths, thereby providing both improved energy and power densities. Impressively, the energy and power densities obtained in the present work could meet the power demands of the PNGV (Partnership for a New Generation of Vehicles) by providing simultaneously high energy and power densities at low cost.

4. Experimental details

4.1 Synthesis of $BiVO_4$ Nanorods anode

Simple surfactant assisted hydrothermal method was used to prepare banana blossom's like $BiVO_4$ nanorods. Briefly, a mixed solvent was prepared by using 65 mL of distilled water and 5 mL of HNO_3 solution (total volume of solution was 70 ml). Later, this solution was equally divided into two beakers. Then 5 mmol of both bismuth(III) nitrate ($Bi(NO_3)_3 \cdot 5H_2O$) and ammonium metavanadate (NH_4VO_3) were separately dissolved in each 35 mL of solvent. Then, 0.72 mmol (0.25 g) of sodium dodecyl benzene sulfonate (SDBS) was added to both of the above solutions and stirred for next 30 min. In the next step, NH_4VO_3 solution was slowly added to $Bi(NO_3)_3 \cdot 5H_2O$ solution under vigorous magnetic stirring for 30 min. Further ammonia solution (NH_4OH) was added in order to adjust the pH of the solution to ≈7. Then the resulting suspension was poured into a Teflon linked stainless steel autoclave and maintained at a temperature of 180°C for 12 hr. The precipitate was collected and washed thoroughly using distilled water followed by ethanol. The obtained product was finally dried at 60°C overnight in the oven and used for further characterization.

4.2 Synthesis of partially reduced graphene oxide (PRGO) cathode

Graphene oxide (GO) was first prepared by modified Hummers method described as follows. 2.5 g of graphite powder was added to the mixture of 2.5 g sodium nitrate ($NaNO_3$) and 110 ml sulfuric acid

(H_2SO_4) and the mixture was stirred in an ice bath for 30 min. Later, 12 g of potassium permanganate ($KMnO_4$) was added to the above solution and the solution was maintained at 50 °C for 2 h with constant stirring. Next, 300 ml of deionized water and 15 ml hydrogen peroxide (H_2O_2, 35%) were then gradually added to the solution. Later, the solution was washed with 500 ml of hydrochloric acid (HCl, 10%). Finally, the GO was washed with extra 200 ml HCl (37%) and deionized water and then dried in vacuum oven at 60 °C overnight. In order to prepare partially reduced graphene oxide (FGO), the GO powder was annealed at 120 °C for 6 h.

4.3 Materials characterization

The surface morphological analyses of samples were carried out using the different techniques such as field-emission scanning electron microscopy (FEI Quanta 650F Environmental SEM) and transmission electron microscopy (Tecnai G2 F20 S-TWIN HR(S) TEM, FEI). The crystal structure analysis was performed with Panalytical X'pert Pro-MRD instrument (Cu Ka radiation and PIXel detector). For Rietveld refinement, FullProf Suite program with VESTA graphical interface was used. The X-ray photoelectron spectra (XPS) analyses were obtained by X-ray photoelectron spectroscopy (XPS, SPECS Germany, PHOIBOS 150). The volumetric capacity of BiVO4 electrode was calculated using formula: Volumetric capacity = bulk density*specific capacity (V_c= ρ* specific capacity), where ρ is the bulk density of $BiVO_4$ (5.2 gm/cm^3).

4.4 Electrochemical testing

Electrodes were prepared by mixing the active material (BiVO4 or partially reduced graphene oxide (PRGO)), Super-P conductive carbon black and polyvinylidene fluoride binder (PVDF) in an N-methyl-2-pyrrolidone (NMP) with 70 %:20 %:10% ratio. The resulting paste was uniformly coated onto Al or Cu foil, dried at 100 °C for 12 h, and pressed under hydraulic press. The mass loading of $BiVO_4$ and PRGO was around 1.5 mg/cm^2. Initially, both the materials $BiVO_4$ and PRGO were tested with half-cell configuration where the Li metal, glass-fiber and a 1 M lithium hexafluorophosphate in a 1:1 mixture of ethylene carbonate and dimethyl carbonate (1:1, EC:DMC) were used as counter electrode, separator and electrolyte, respectively. The PRGO cathode half-cell was tested within the voltage range from 4.5 to 1.5

V and $BiVO_4$ anode within 3.0 to 0.01 V using a Biologic potentio-galvanostat. Prior to assembling full LIC cell, $BiVO_4$ and PRGO were cycled 10 cycles in half-cells at 0.1 A/g, and then the cells were disassembled in the glove box and by collecting electrodes, full cell was fabricated and tested within 0.01 to 4 V. The $BiVO_4$ anode was fully discharged up to 0.01 V (vs. Li) before used in the full LIC cells. In present investigation, the mass ratio of $BiVO_4$ to PRGO was maintained at 1:5 (1.6 mg of $BiVO_4$ and 7.9 mg of PRGO). We have used following equations for calculation of capacitance and conversion in to capacity.

$$C\left(\frac{F}{g}\right) = \frac{i\,(A) \times t\,(s)}{3600 \times m\,(g)} = \frac{mAh}{g} \times \frac{3600}{dV\,(mV)} \quad (4)$$

where, i is the applied current, t is the discharge time, m is the weight of the active material and d V is the testing potential window of the single electrode configuration (mV). The energy density (E) and power density (P) of the Li-ion hybrid capacitor are calculated using following equations, respectively.

$$P = \frac{\Delta V \times i}{m} \quad (5)$$

$$E = \frac{P \times t}{3600} \quad (6)$$

$$\Delta V = \frac{E_{max} + E_{min}}{2} \quad (7)$$

Acknowledgments

DPD acknowledges the support of University of Adelaide, Australia for grant of Research Fellowship (Research for Impact) and the Secretary for Universities and Research of the Ministry of Economy and Knowledge of the Government of Catalonia and the Co-fund program of the Marie Curie Actions of the 7th R&D Framework Program of the European Union. K. J. R. is grateful to the Alexander von Humboldt (AvH) foundation for a post-doctoral fellowship. The authors also gratefully acknowledge support by the Catalysis Research Centre at TU Munich and the support from the Ministry of Education, Youth and Sports of the Czech Republic (LO1305) and the assistance provided by the Research Infrastructure NanoEnviCz, supported by the Ministry of Education, Youth and Sports of the Czech Republic under Project No. LM2015073.

5. References

[1] M. Armand, J. M. Tarascon, *Nature*, **2008**, *451*, 652.

[2] A. S. Aricò, P. Bruce, B. Scrosati, J. -M. Tarascon, W. Van Schalkwijk, *Nat. Mater.* **2005**, *4*, 366.

[3] Y. Gogotsi, P. Simon, *Science*, **2011**, *334*, 917

[4] V. Aravindan, J. Gnanaraj, Y.-S. Lee, M. Srinivasan, *Chem. Rev.* **2014**, *114*, 11619

[5] D. P. Dubal, O. Ayyad, V. Ruiz, P. Gómez-Romero, *Chem. Soc. Rev.* **2015**, *44*, 1777

[6] K. Naoi, W. Naoi, S. Aoyagi, J. Miyamoto, T. Kamino, *Acc. Chem. Res.*, **2013**, *46*, 1075

[7] K. Naoi, S. Ishimoto, J.-i. Miyamoto, W. Naoi, *Energy Environ. Sci.* **2012**, *5*, 9363

[8] Y. Ma, H. Chang, M. Zhang, Y. Chen, *Adv. Mater.* **2015**, *27*, 5296

[9] K. Naoi, P. Simon, *J. Electrochem. Soc.* **2008**, *17*, 34

[10] E. Frackowiak, F. Beguin, *Carbon* **2001**, *39*, 937

[11] P. Simon, P. L. Taberna, F. Beguin, Wiley-VCH, Weinheim, 2013, p. 131

[12] K. Naoi, *Fuel Cells* **2010**, *10*, 825

[13] K. Naoi, S. Ishimoto, Y. Isobe, S. Aoyagi, *J. Power Sources* **2010**, *195*, 6250

[14] V. Aravindan, M. V. Reddy, M. Srinivasan, S. G. Mhaisalkar, G. V. Subba Rao, B. V. R. Chowdari, *J. Power Sources* **2011**, *196*, 8850

[15] H. Kim, M. Y. Cho, M. H. Kim, K. Y. Park, H. Gwon, Y. Lee, K. C. Roh, K. Kang, *Adv. Energy Mater*. **2013**, *3*, 1500

[16] V. Aravindan, W. Chuiling, M. Srinivasan, *J. Mater. Chem.* **2012**, *22*, 16026

[17] S. Patoux, C. Masquelier, *Chem. Mater.* **2002**, *14*, 5057

[18] (a) D. P. Dubal, D. R. Patil, S. S. Patil, N. R. Munirathnam, P. Gomez-Romero, *ChemSusChem* **2017**, 10, 4163, (b) S. B. Ni, X. H. Lv, J. J. Ma, X. L. Yang, L. L. Zhang, *J. Power Sources* **2014**, *248*, 122

[19] D. H. Sim, X. Rui, J. Chen, H. Tan, T. M. Lim, R. Yazami, H. H. Hng, Q. Yan, *RSC Adv*, **2012**, *2*, 3630

[20] H. W. Liu, D. G. Tang, *Mater. Chem. Phys.* **2009**, *114*, 656

[21] S. B. Ni, J. J. Ma, J. J. Zhang, X. L. Yang, L. L. Zhang, *Chem. Commun.* **2015**, *51*, 5880

[22] H. Q. Li, X. Z. Liu, T. Y. Zhai, D. Li, H. S. Zhou, *Adv. Energy Mater.* **2013**, *3*, 428

[23] Y. Shi, J. Z. Wang, S. L. Chou, D. Wexler, H. J. Li, K. Ozawa, H. K. Liu, Y. P. Wu, *Nano Lett.* **2013**, *13*, 4715

[24] W. T. Kim, Y. U. Jeong, Y. J. Lee, Y. J. Kim, J. H. Song, *J. Power Sources* **2013**, *244*, 557

[25] N. Yan, Y. X. Hongjun, L. W. Chen, *Mater. Lett.*, **2016**, *165*, 223

[26] S. S. Patil, D. P. Dubal, M. S. Tamboli, J. D. Ambekar, S. S. Kolekar, P. Gomez-Romero,

B. B. Kale, D. R. Patil, *J. Mater. Chem. A*, **2016**, *4*, 7580

[27] S. S. Patil, D. P. Dubal, V. G. Deonikar, M. S. Tamboli, J. D. Ambekar, P. Gomez-Romero, S. S. Kolekar, B. B. Kale, D. R. Patil, *ACS Appl. Mater. Interfaces* **2016**, *8*, 31602

[28] M. R. Palacin, *Chem. Soc. Rev.*, **2009**, *38*, 2565

[29] M. Pasquali, G. Pistoia, *J. Power Sources*, **1989**, *27*, 29

[30] H. Kim, H. D. Lim, S. W. Kim, J. Hong, D. H. Seo, D. Kim, S. Jeon, S. Park, K. Kang, *Sci. Rep.* **2013**, *3*, 1506

[31] H. Kim, K. Y. Park, J. Hong, K. Kang, *Sci. Rep.* **2014**, *4*, 5278

[32] Z. Zhao, Z. Li, Z. Zou, *RSC Advances*, **2011**, *1*, 874

[33] Z. Zhao, Z. Li, Z. Zou, *Phys. Chem. Chem. Phys.,* **2011**, *13*, 4746

[34] T. W. Kim, Y. Ping, G. A. Galli, K. S. Choi, *Nat. Commun.* **2015**, *6*, 8769

[35] L. L. Zhou, S. Y. Shen, X. Peng, L. N. Wu, Q. Wang, C. H. Shen, T. T. Tu, L. Huang, J. T. Li, S. G. Sun, *ACS Appl. Mater. Interfaces*, **2016**, *8*, 23739

[36] Y. Li, M. A. Trujillo, E. Fu, B. Patterson, L. Fei, Y. Xu, S. Deng, S. Smirnov, H. Luo, *J. Mater. Chem. A*, **2013**, *1*, 12123

[37] H. Su, Y. F. Xu, S. C. Feng, Z. G. Wu, X. P. Sun, C. H. Shen, J. Q. Wang, J. T. Li, L. Huang, S. G. Sun, *ACS Appl. Mater. Interfaces* **2015**, *7*, 8488

[38] S. Ni, J. Zhang, J. Ma, X. Yang, L. Zhang, *J. Power Sources* **2015**, *296*, 377

[39] H. Li, X. Liu, T. Zhai, D. Li, H. Zhou, *Adv. Energy Mater.* **2013**, *3*, 428

[40] L. Chen, X. Jiang, N. Wang, J. Yue, Y. Qian, J. Yang, *Adv. Sci.* **2015**, *2*, 1500090

[41] L. L. Zhou, S. Y. Shen, X. Peng, L. N. Wu, Q. Wang, C. H. Shen, T. T. Tu, L. Huang, J. T. Li, S. G. Sun, *ACS Appl. Mater. Interfaces*, **2016**, *8*, 23739

[42] N. Yan, Y. Xu, H. Li, W. Chen, *Mater. Lett.* **2016**, *165*, 223

[43] C. Zhang, C. Liu, X. Nan, H. Song, Y. Liu, C. Zhang, G. Cao, *ACS Appl. Mater. Interfaces*, **2016**, *8*, 680

[44] Z. Chen, V. Augustyn, X. Jia, Q. Xiao, B. Dunn, Y. Lu, *ACS Nano* **2012**, *6*, 4319.

[45] Y. Yang, J. Li, D. Chen, J. Zhao, *J. Electrochem. Soc.* **2017**, *164*, A6001

[46] D. Su, S. Dou, G. Wang, *Nano Energy* **2015,** *12*, 88

[47] Q. Wang, Z. Wen, J. Li, *Adv. Funct. Mater.* **2006**, *16*, 2141

[48] V. Aravindan, D. Mhamane, W. C. Ling, S. Ogale, S. Madhavi, *ChemSusChem* **2013**, *6*, 2240

[49] A. Banerjee, K. K. Upadhyay, D. Puthusseri, V. Aravindan, M. Srinivasan, S. Ogale, *Nanoscale* **2014**, *6*, 4387

[50] (a) G. P. Kim, S. Park, I. Nam, J. Park, J. Yi, *J. Power Sources* **2013**, *237*, 172. (b) P.

Simon, Y. Gogotsi, *Nat. Mater.* **2008**, *7*, 845.

[51] E. Lim, C. Jo, H. Kim, M. H. Kim, Y. Mun, J. Chun, Y. Ye, J. Hwang, K. S. Ha, K. C. Roh, K. Kang, S. Yoon, J. Lee, *ACS Nano* **2015**, 9, 7497-7505

[52] R. Yi, S. Chen, J. Song, M. L. Gordin, A. Manivannan, D. Wang, *Adv. Funct. Mater.* **2014**, *24*, 7433

[53] H. Wang, C. Guan, X. Wang, H. J. Fan, *Small* **2015**, *11*, 1470

[54] K. Karthikeyan, S. Amaresh, S. N. Lee, V. Aravindan, Y. S. Lee, *Chem. Asian J.* **2014**, *9*, 852

[55] K. Leng, F. Zhang, L. Zhang, T. Zhang, Y. Wu, Y. Lu, Y. Huang, Y. Chen, *Nano Research* **2013**, *6*, 581

[56] X. Wang, P. S. Lee, *J. Mater. Chem. A,* **2015**, *3*, 21706

[57] H. Wang, Y. Zhang, H. Ang, Y. Zhang, H. T. Tan, Y. Zhang, Y. Guo, J. B. Franklin, X. L. Wu, M. Srinivasan, H. J. Fan, Q. Yan, *Adv. Funct. Mater* **2016**, *26*, 3082

Figure captions

Figure 1 (a) Rietveld-refined XRD pattern of $BiVO_4$ nanorods, (b) The crystal structure of monoclinic clinobisvanite $BiVO_4$ and corresponding polyhedron structure (VO_4 tetrahedron in red, and BiO_8 dodecahedron in purple). (c and d) Core-level XPS spectra for Bi4f and V2p, respectively.

Figure 2 (a, b) SEM and (c) TEM images of $BiVO_4$ nanorods, respectively, (d, e) HRTEM image of single $BiVO_4$ nanorod with corresponding inverse fast Fourier Transform (FFT) image of the selected area shown by white rectangle (d) SAED pattern of $BiVO_4$, confirming the formation of monoclinic clinobisvanite.

Figure 3 Electrochemical properties of $BiVO_4$ nanorods in Li-half cell configuration: (a) First few cyclic voltammetry (CV) curves measured at 1 mV/s scan rate, (b) Initial eight charge/discharge curves measured at 1.1 A/g, (c) Variation of specific and volumetric capacities with number of cycles at different current densities (d) Cycling stability and Coulombic efficiency over 500 cycles at 1.1 A/g, showing excellent capacity retention over 500 cycles. (e) The capacitive charge in total charge storage of $BiVO_4$ electrode at different scan rates (f) Li-ion diffusion coefficients at different scan rates and different peaks.

Figure 4 (a) *Ex-situ* XRD patterns of electrodes at different charge and discharge potentials, (b) *Ex-situ* XRD patterns of electrodes at different charge/discharge cycles, (c) *Ex-situ* magnified XPS spectra of Bi4f and V2p, respectively.

Figure 5 (a) FESEM of PRGO, showing highly porous, interconnected nanosheets network. (b-d) Electrochemical properties of partially reduced graphene oxide (PRGO) cathode in a Li half-cell within the potential range of 1.5 to 4.5 V (vs Li/Li^+). (b) Galvanostatic charge/discharge curves at different rates, (c) variation of specific capacitance and specific capacity with current densities, (d) Cycle life performance and Coulombic efficiency measured over 4000 cycles at 0.9 A/g

Figure 6 Electrochemical properties of $BiVO_4$//PRGO LIC cell in voltage range of 0.01 to 4 V; (a) Typical charge/discharge curves for $BiVO_4$//PRGO cell, inset shows magnified view of CD curves at high current densities, (b) CD curve for $BiVO_4$//PRGO LIC cell at current density of 1.1 A/g with corresponding potential distribution across $BiVO_4$ anode and PRGO cathode versus Li-foil reference electrode, (c) Rate capability of $BiVO_4$//PRGO cell at different current densities (d) Variation of specific capacitance and capacity with current density for $BiVO_4$//PRGO cell. (e) Ragone plot for $BiVO_4$//PRGO device with comparison of previously reported values (the values and references are provided in supporting information S.I. Table 2) (f) Capacity retention and Coulombic efficiency of $BiVO_4$//PRGO LIC cell over 6000 cycles, suggesting excellent cycling stability with >98 % Coulombic efficiency.

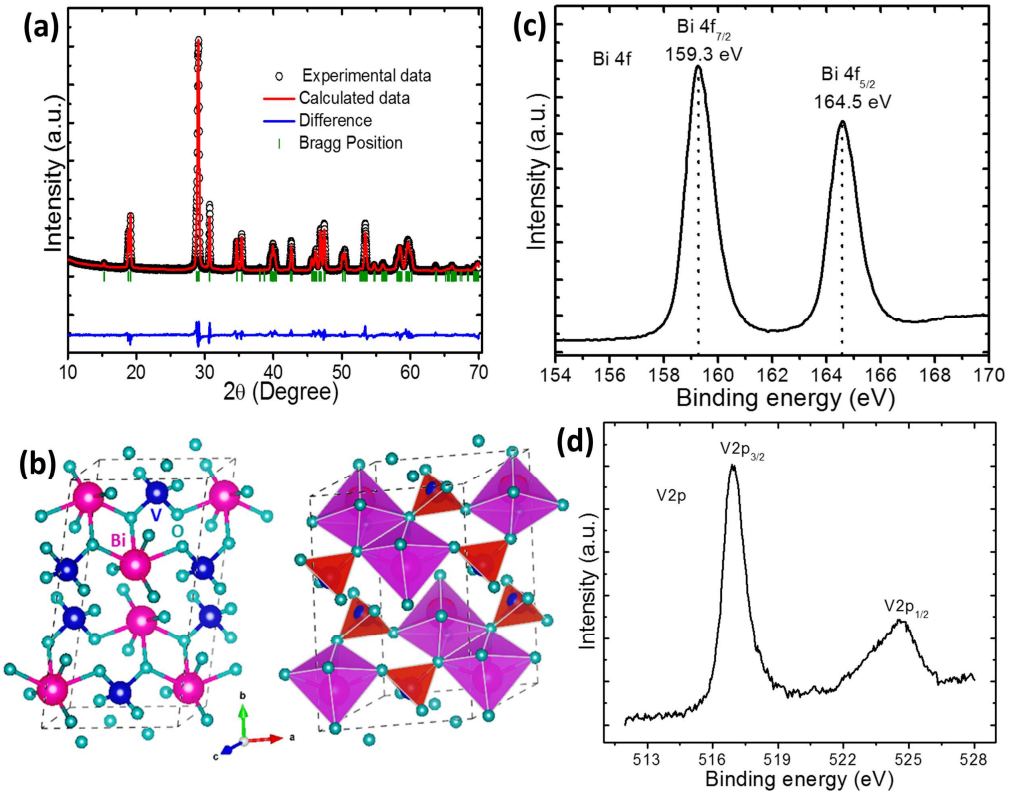
(a)
Intensity (a.u.)
Experimental data
Calculated data
Difference
Bragg Position
10 20 30 40 50 60 70
2θ (Degree)
(c)
Bi 4f
Bi 4f7/2
159.3 eV
Bi 4f5/2
164.5 eV
Intensity (a.u.)
154 156 158 160 162 164 166 168 170
Binding energy (eV)
(b)
Bi
V
O
b
a
c
(d)
V2p3/2
V2p
V2p1/2
Intensity (a.u.)
513 516 519 522 525 528
Binding energy (eV)

Figure 1

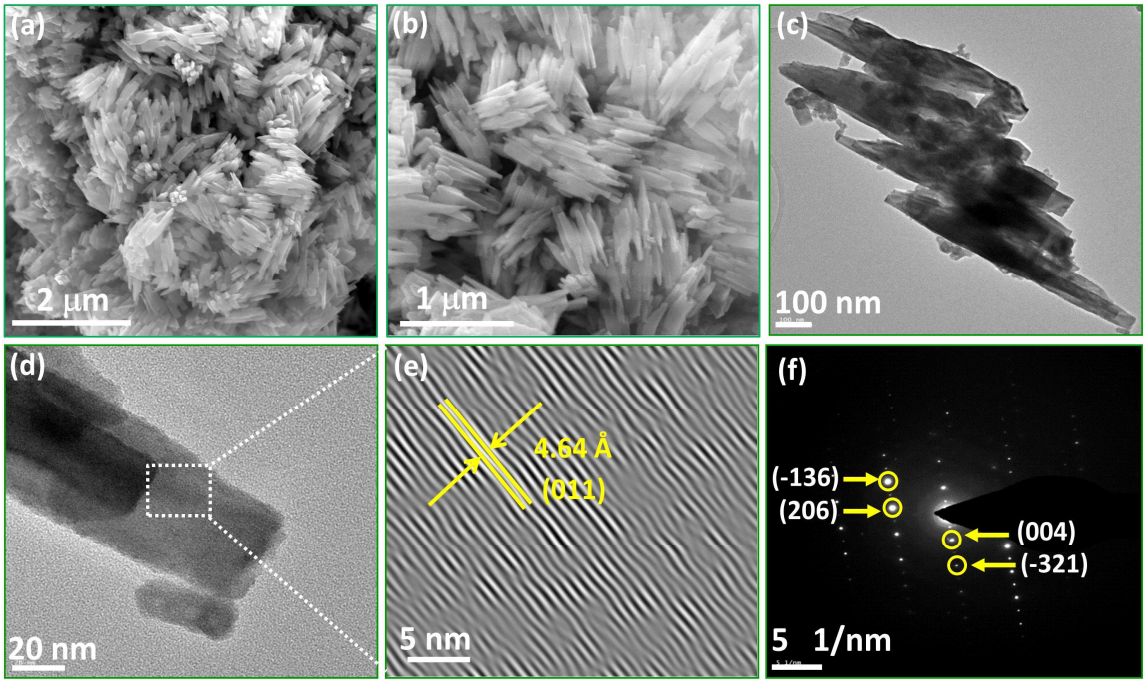

Figure 2

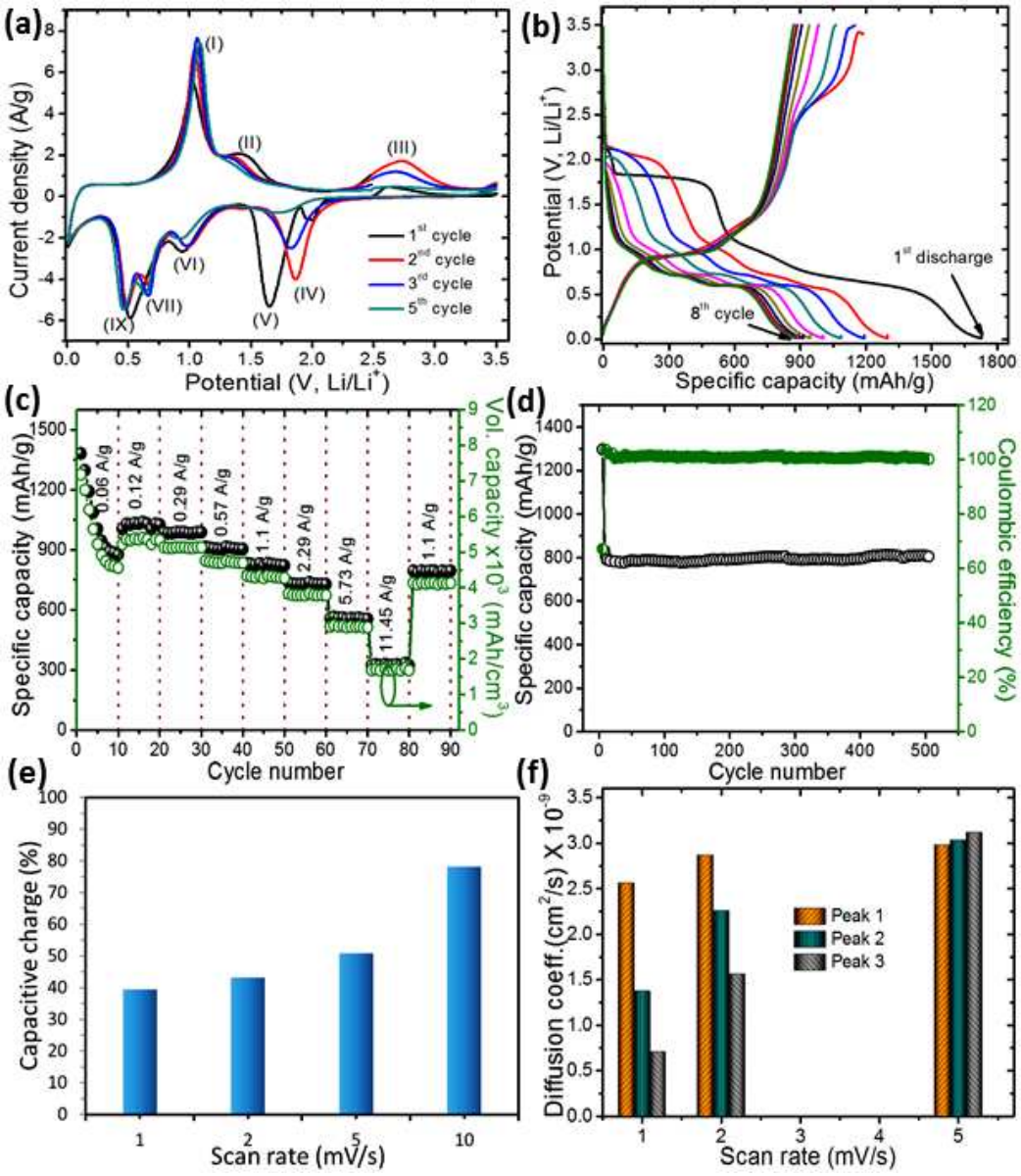
(a)
Current density (A/g)
Potential (V, Li/Li+)
(I)
(II)
(III)
(IV)
(V)
(VI)
(VII)
(IX)
1st cycle
2nd cycle
3rd cycle
5th cycle
(b)
Potential (V, Li/Li+)
Specific capacity (mAh/g)
1st discharge
8th cycle
(c)
Specific capacity (mAh/g)
Vol. capacity x10^3 (mAh/cm^3)
Cycle number
0.06 A/g
0.12 A/g
0.29 A/g
0.57 A/g
1.1 A/g
2.29 A/g
5.73 A/g
11.45 A/g
1.1 A/g
(d)
Specific capacity (mAh/g)
Coulombic efficiency (%)
Cycle number
(e)
Capacitive charge (%)
Scan rate (mV/s)
(f)
Diffusion coeff.(cm2/s) X 10-9
Peak 1
Peak 2
Peak 3
Scan rate (mV/s)

Figure 3

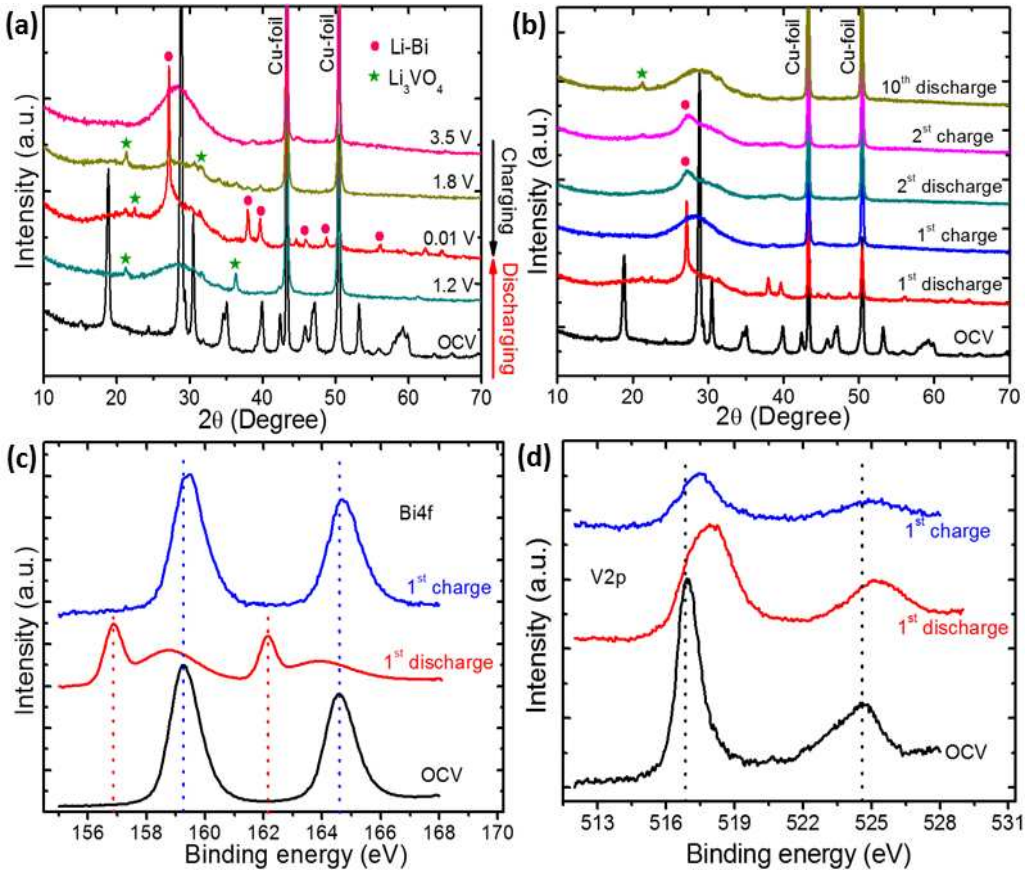
(a)
Cu-foil
Cu-foil
Li-Bi
Li3VO4
3.5 V
1.8 V
0.01 V
1.2 V
OCV
Charging
Discharging
Intensity (a.u.)
2θ (Degree)
(b)
Cu-foil
Cu-foil
10th discharge
2st charge
2st discharge
1st charge
1st discharge
OCV
Intensity (a.u.)
2θ (Degree)
(c)
Bi4f
1st charge
1st discharge
OCV
Intensity (a.u.)
Binding energy (eV)
(d)
V2p
1st charge
1st discharge
OCV
Intensity (a.u.)
Binding energy (eV)

Figure 4

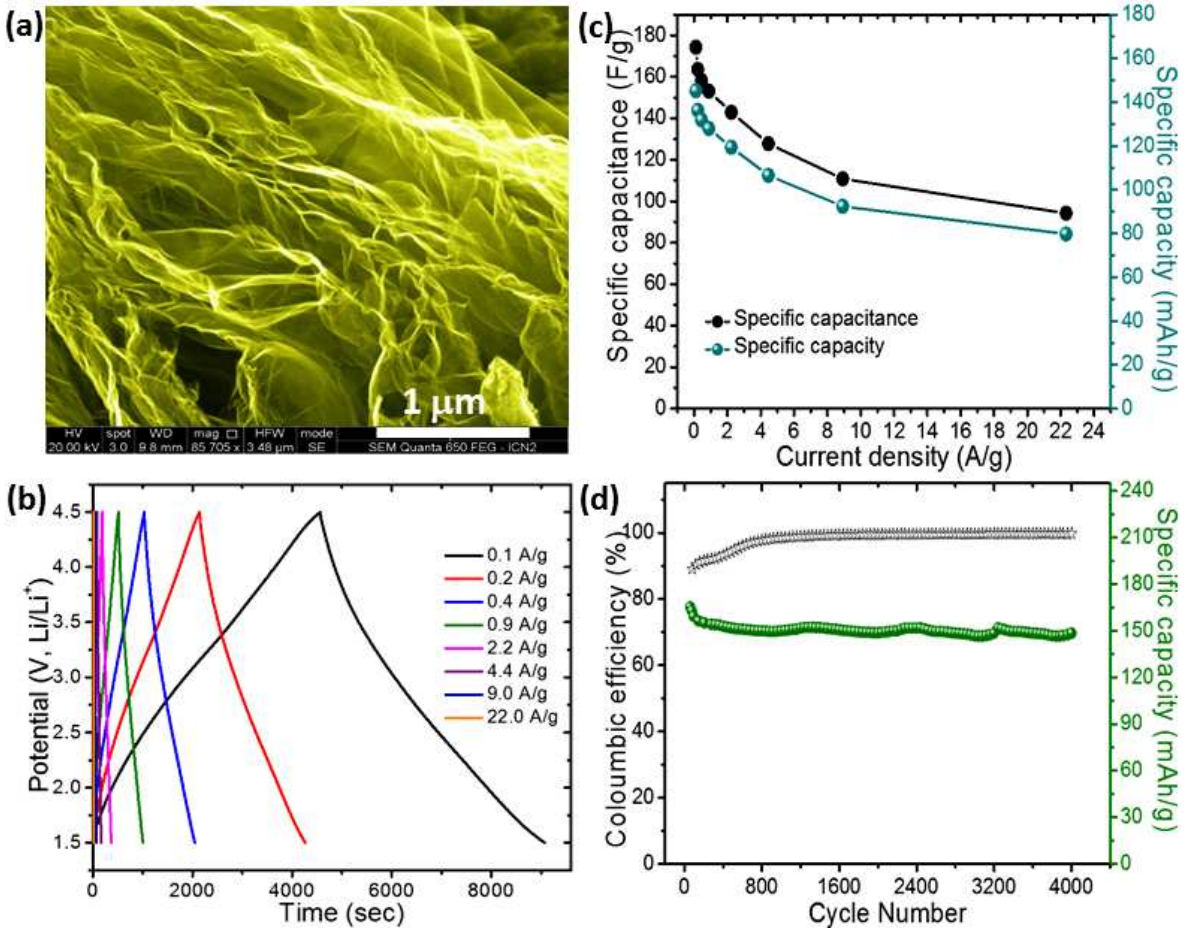
(a)
1 µm
HV spot WD mag HFW mode
20.00 kV 3.0 9.8 mm 85 705 x 3.48 µm SE
SEM Quanta 650 FEG - iCN2
(c)
Specific capacitance (F/g)
Specific capacity (mAh/g)
Current density (A/g)
Specific capacitance
Specific capacity
(b)
Potential (V, Li/Li+)
Time (sec)
0.1 A/g
0.2 A/g
0.4 A/g
0.9 A/g
2.2 A/g
4.4 A/g
9.0 A/g
22.0 A/g
(d)
Coloumbic efficiency (%)
Specific capacity (mAh/g)
Cycle Number

Figure 5

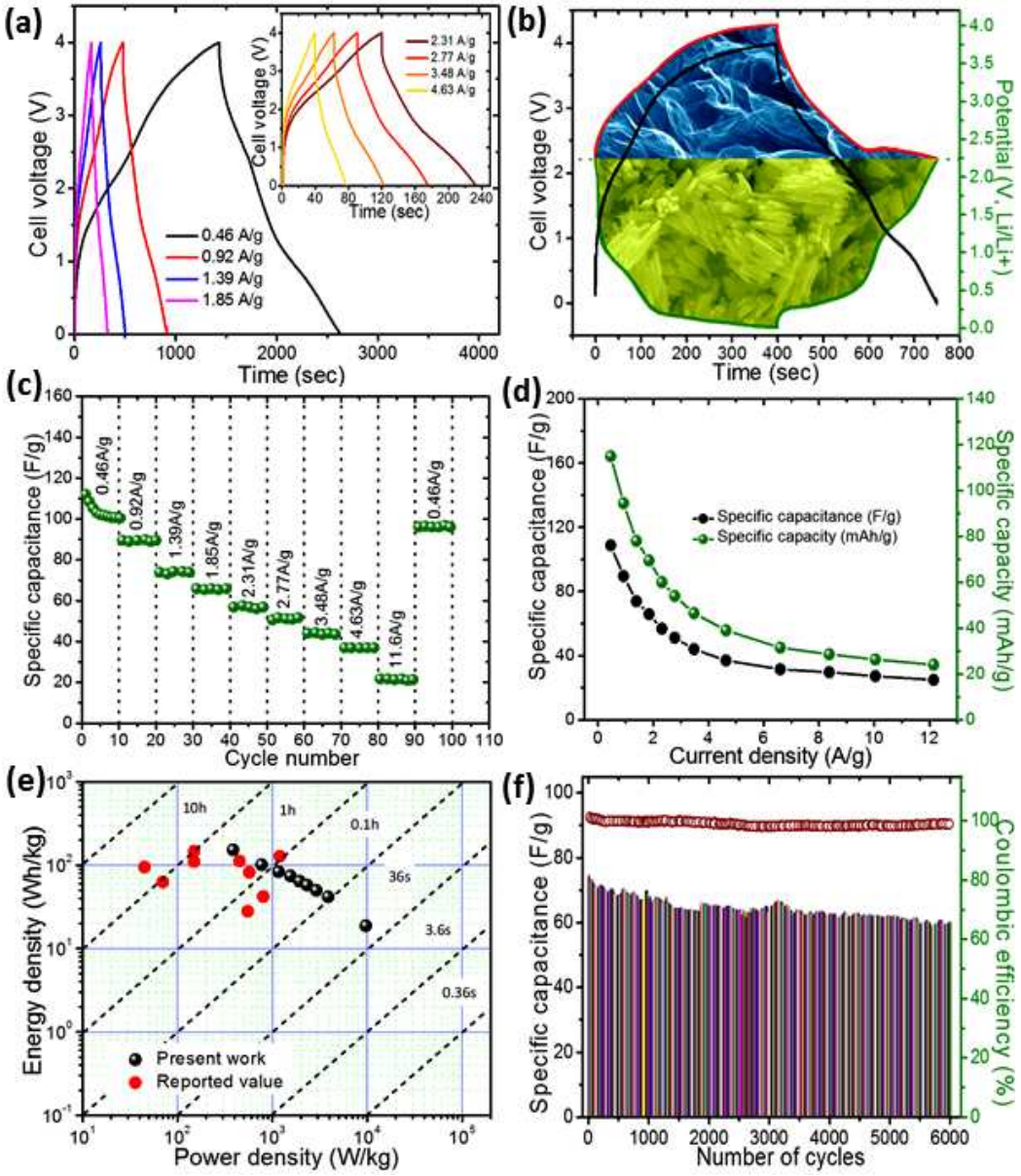
(a)
Cell voltage (V)
Time (sec)
0.46 A/g
0.92 A/g
1.39 A/g
1.85 A/g
2.31 A/g
2.77 A/g
3.48 A/g
4.63 A/g
(b)
Cell voltage (V)
Potential (V, Li/Li+)
Time (sec)
(c)
Specific capacitance (F/g)
Cycle number
0.46A/g
0.92A/g
1.39A/g
1.85A/g
2.31A/g
2.77A/g
3.48A/g
4.63A/g
11.6A/g
0.46A/g
(d)
Specific capacitance (F/g)
Specific capacity (mAh/g)
Current density (A/g)
(e)
Energy density (Wh/kg)
Power density (W/kg)
10h
1h
0.1h
36s
3.6s
0.36s
Present work
Reported value
(f)
Specific capacitance (F/g)
Coulombic efficiency (%)
Number of cycles

Figure 6

TOC

Graphical Abstract

A high energy and high power density Li-ion capacitor based on $BiVO_4$ Nanorods (left) and partially reduced graphene oxide nanosheets (PRGO, on right) for EV applications.

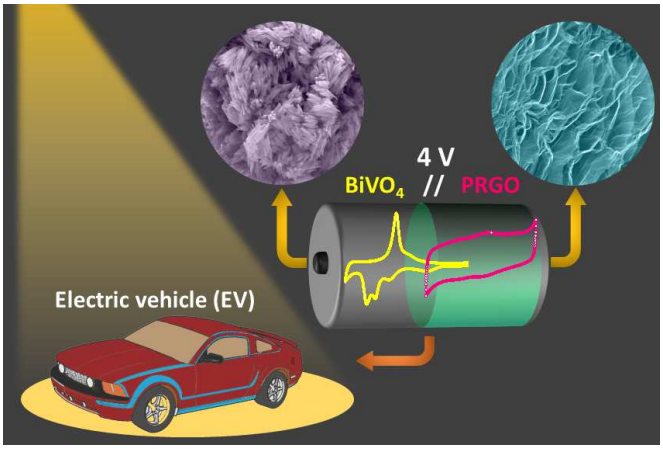

Supporting Information

Unveiling $BiVO_4$ Nanorods as a Novel Anode Material for High Performance Lithium Ion Capacitor: Beyond Intercalation Strategy

Deepak P. Dubal,[a, b] Kolleboyina Jayaramulu,[c,d] Radek Zboril,[d] Roland A. Fischer,[c] Pedro Gomez-Romero [b]**

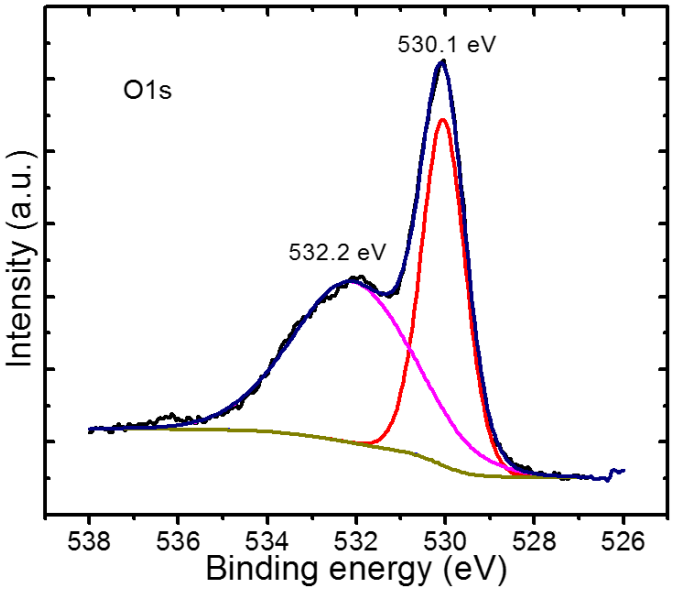

Figure S1 Magnified XPS spectrum for O1s of $BiVO_4$ nanorods with deconvulated peaks.

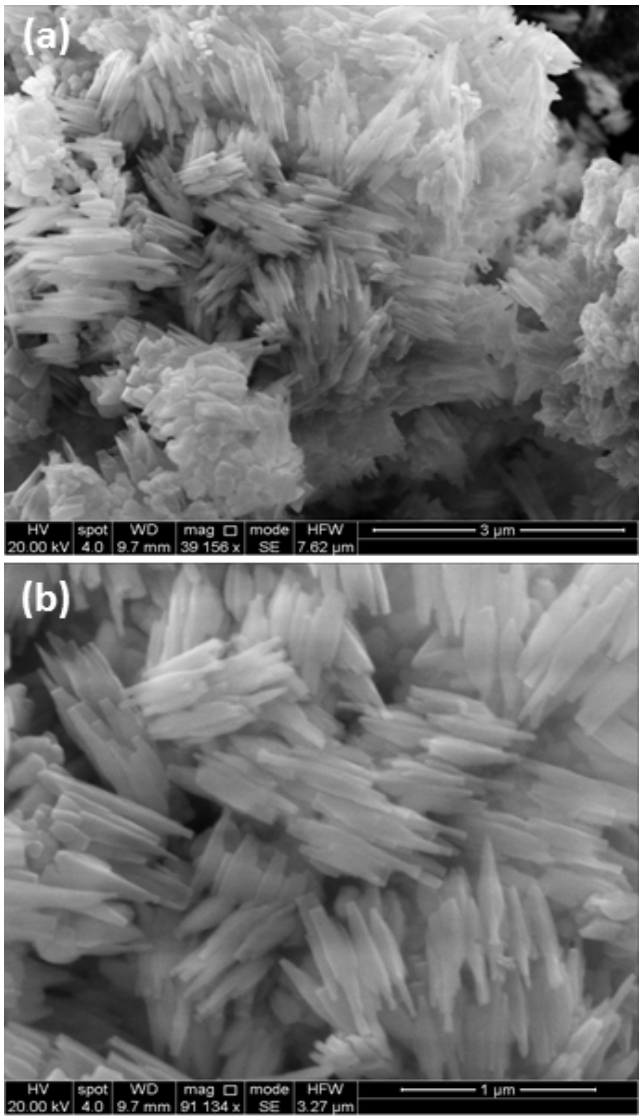

Figure S2 SEM images of $BiVO_4$ nanorods at two different magnifications.

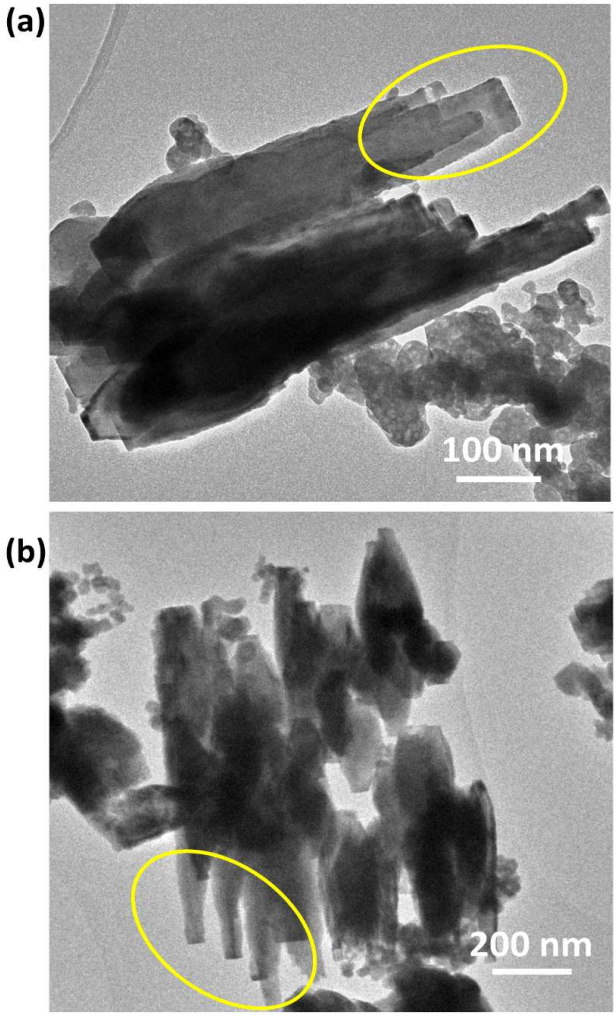

Figure S3 TEM images of $BiVO_4$ nanorods at two different magnifications, suggesting the formation of nanorods.

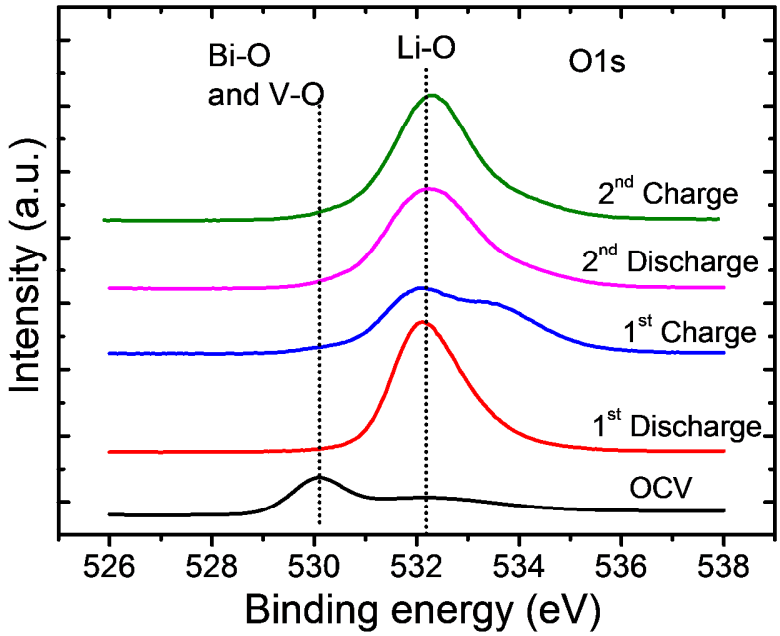

Figure S4 Ex-situ XPS analysis: core-level O1s spectra of $BiVO_4$ electrode after charge/discharge cycles, suggesting the presence of Bi-O, V-O and Li-O.

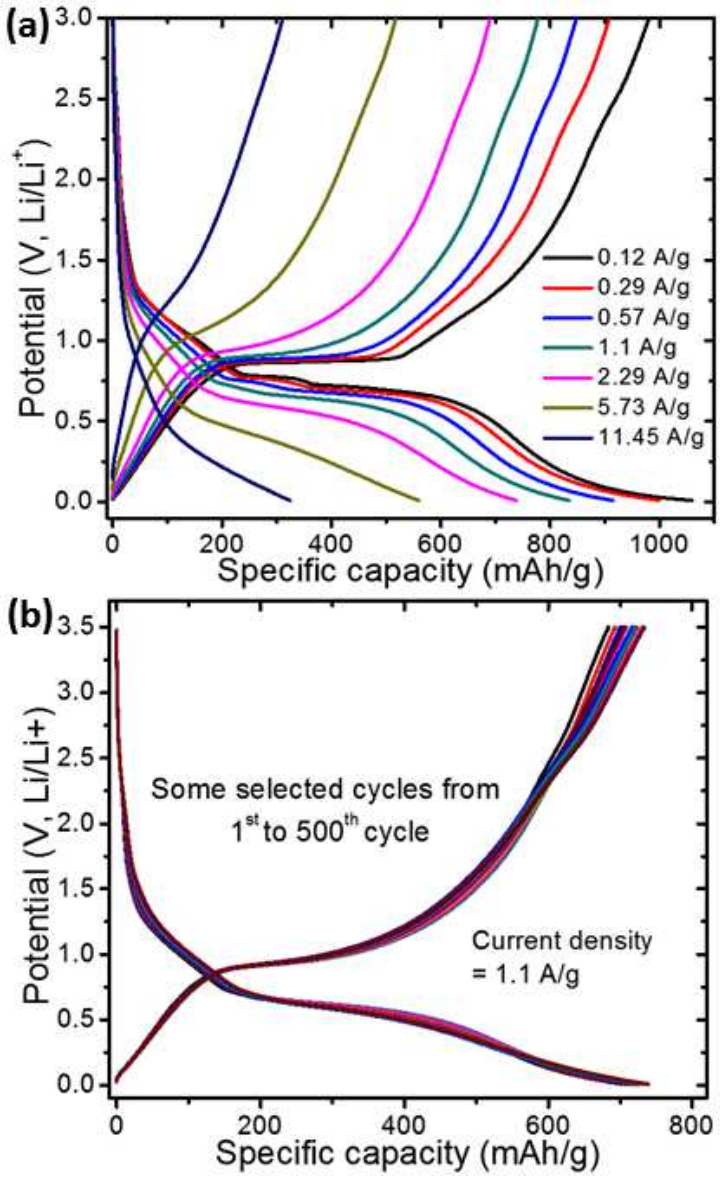

Figure S5 (a) Galvanostatic charge/discharge curves for $BiVO_4$ nanorods in half-cell configuration at different current densities, (b) Few galvanostatic charge/discharge cycles from 500 cycles measured at 1.1 A/g

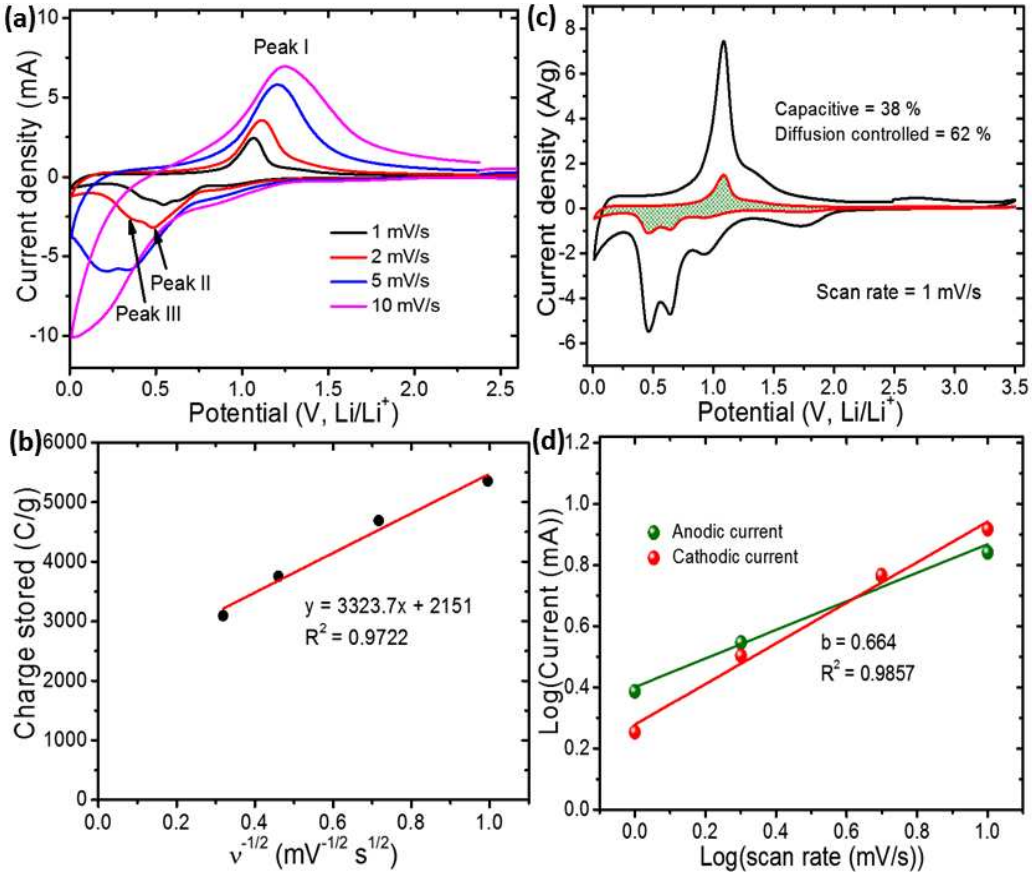

Figure S6 (a) Cyclic voltammetry curves for $BiVO_4$ anode at different scan rates, (b) The plot of total gravimetric charge against the reciprocal of the square root of potential scan rate for $BiVO_4$ electrodes, (c) Voltammetric response at a scan rate of 1 mV/s, the capacitive contribution to the total current is shown by the shaded region, (d) Plot of log (current) vs log(scan rate) for anodic and cathodic responses.

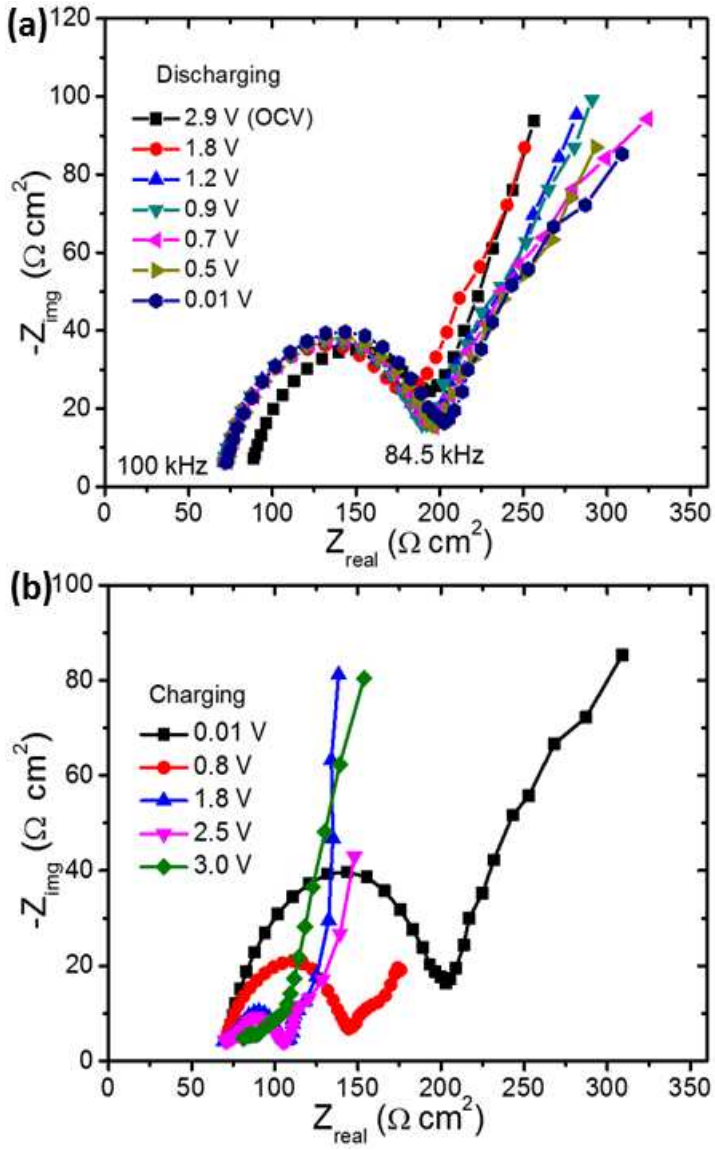

Figure S7 Nyquist plots for $BiVO_4$ anode at differetnt discharging (a) and charging (a) potentials.

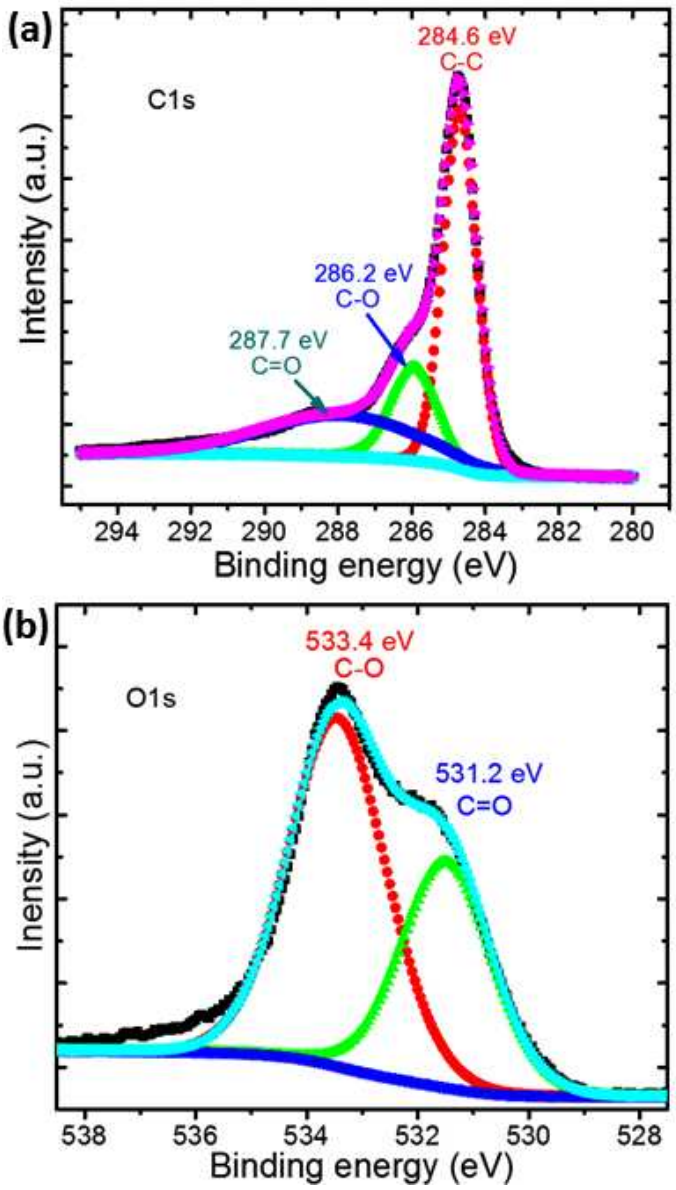

Figure S8 Core-level XPS spectra for (a) C1s and (b) O1s of partially reduced graphene oxide (PRGO) with corresponding deconvulated peaks.

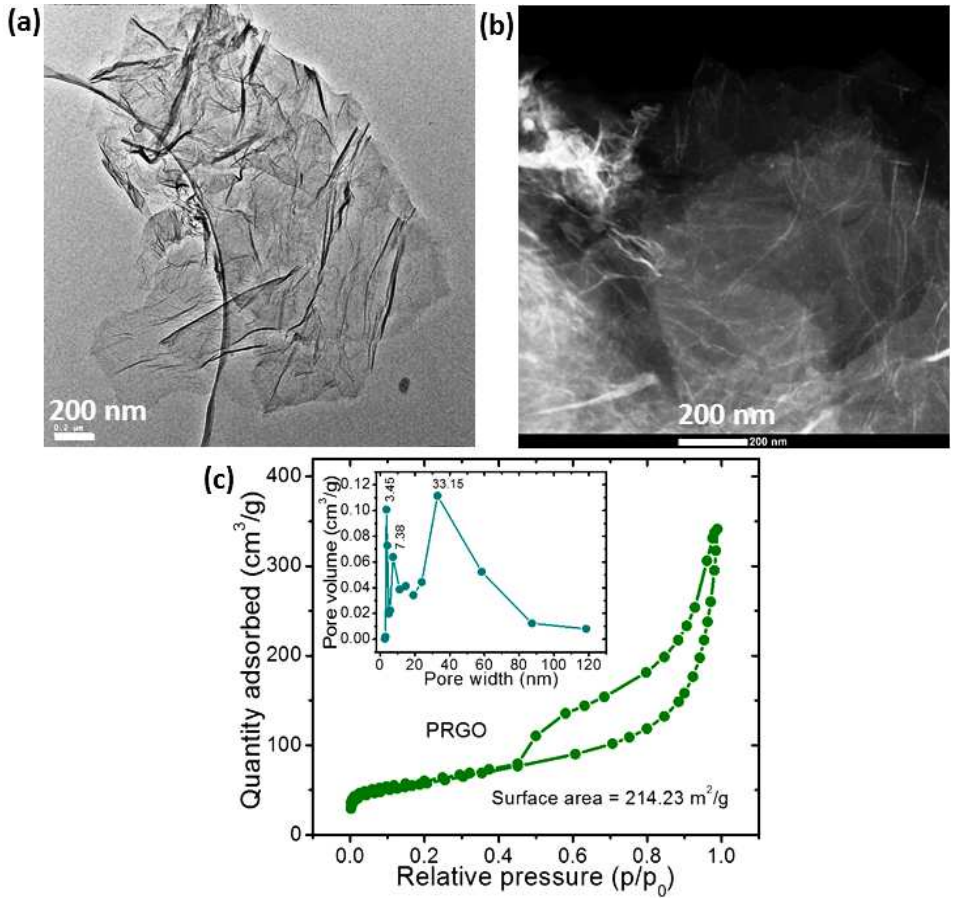

Figure S9 (a) SEM and (b) STEM images of PRGO suggesting the formation of open-porous nanosheets, (c) Nitrogen adsorption/desorption isotherm of PRGO samples with corresponding pore size distribution curves (inset)

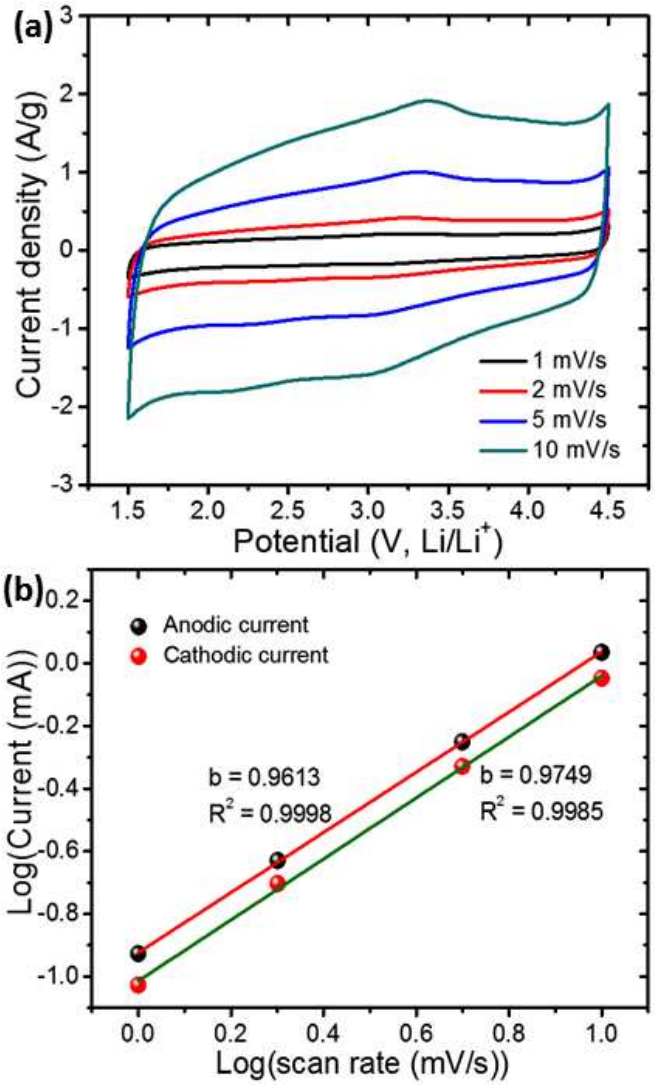

Figure S10 (a) Cyclic voltammetry curves for PRGO cathode at different scan rates (b) Plots of Log(current) vs Log(scan rate) suggesting the major contribution from suface capacitive processes as b ≈ 0.97.

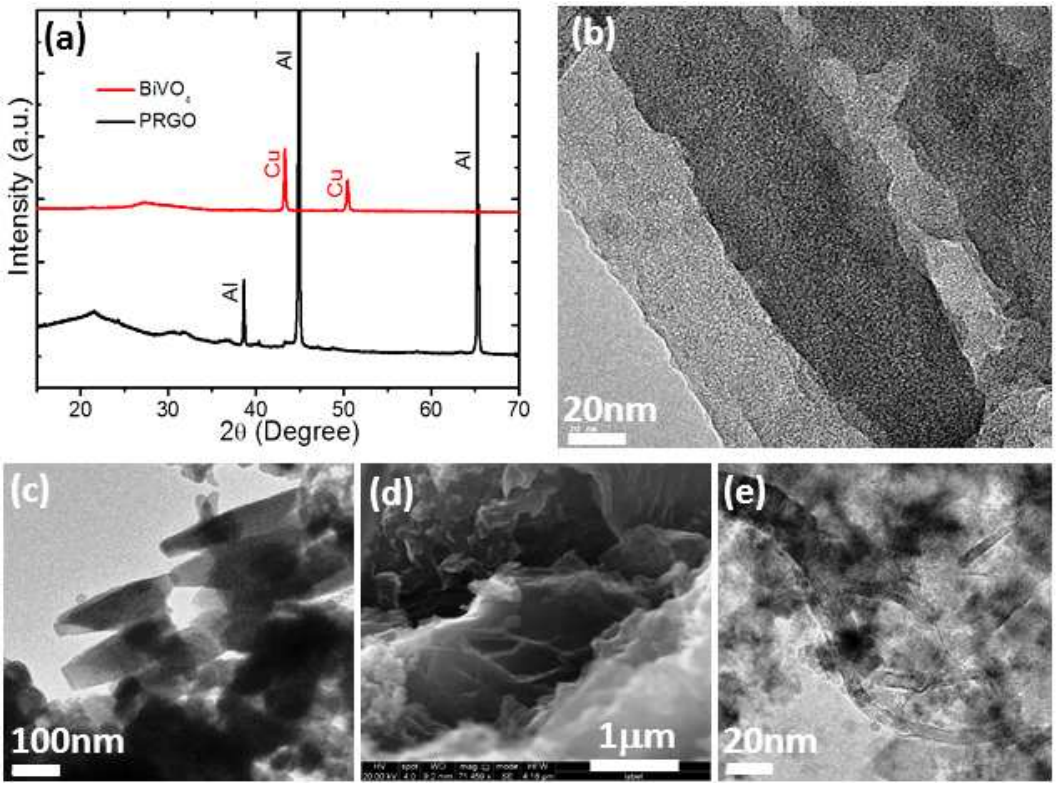

Figure S11 (a) XRD patterns of $BiVO_4$ and PRGO after 6000 cycles, suggesting amorphous nature of the materials. (b and c) TEM images of $BiVO_4$ after 6000 cycles, indicating that $BiVO_4$ still preserves their nanorods-like morphology. (d and e) SEM and TEM image of PRGO after 6000 cycles, respectively. The images suggests that the PRGO maintained their nanosheets-like structure after charge/discharge cycles.

Table S1 Comparison of electrochemical properties of carbon based anode materials with present report

Anode Material	Reversible capacity (mAh/g)	Capacity retention (mAh/g)	Refere
$BiVO_4$	1035 at 0.12 A/g (5382 mAh/cm^3)	793 at 1.1 A/g after 500 cycles	Presen
$FeVO_4$	1237 at 0.5 A/g (4490 mAh/cm^3)	1237 at 0.5 A/g after 100 cycles	[1]
$FeVO_4$	527 at 0.075 A/g	432 at 0.075 after 100 cycles	[2]
$FeVO_4$-graphene	1046 at 0.1 A/g	1046 at 0.1 A/g after 100 cycles	[3]
Li_3VO_4	323 at 0.02 A/g	283 at 0.02 A/g after 25 cycles	[4]
Li_3VO_4/ N-doped graphene	491 at 0.1 A/g	195 at 2 A/g after 900 cycles	[5]
$Li_3VO_{4-\delta}$	416 at 0.2 A/g	286 at 0.2 A/g after 200 cycles	[6]
Li_3VO_4	422 at 0.394 A/g	376 at 0.394 after 75 cycles	[7]
Li_3VO_4/C/CNTs	397 at 0.394 A/g	272 at 4 A/g after 500 cycles	[8]
Hollow-Cuboid Li_3VO_4/C	415 at 0.2 A/g	415 at 0.2 A/g after 50 cycles 92 % retention after 1000 cycles (10 C = 4 A/g)	[9]
Oxygen deficient Li_3VO_4	495 at 0.1 A/g	270 at 1 A/g after 500 cycles	[10]
Li_3VO_4/C/rGO	435 at 0.4 A/g	325 at 4 A/g (10 C) after 5000 cycles (82.5 % retention)	[11]
Li_3VO_4/rGO	486 at 0.4 A/g	163 at 2 A/g after 5000 cycles (63.1 % retention)	[12]
Carbon-Encapsulated Li_3VO_4	410 at 0.4 A/g	80 % capacity retention after 2000 cycles	[13]
Li_3VO_4	481 at 0.1 A/g	398 at 0.1 A/g after 100 cycles	[14]
Li_3VO_4/C hollow spheres	429 at 0.08 A/g	275 at 4 A/g after 3000 cycles (97 % retention)	[15]
Ce doped $FeVO_4$	1339 at 0.09 A/g	513 at 0.09 A/g after 40 cycles	[16]

Table S2 Comparison of published electrochemical properties of Li-ion capacitors with our present work

LIC cell	Energy density (Wh/kg)	Power density (W/kg)	Voltage (V)	Cycling stability	Refe
$BiVO_4$//PRGO	152 at 384 W/kg	3861 at 42 Wh/kg	4.0	79 % after 4000 cycles	Prese
$Li_4Ti_5O_{12}$//AC[2]	67.5 at 490 W/kg	4995 at 33.6 Wh/kg	3.0	85 % after 2000 cycles	[17]
Graphene//FRGO[3]	148.3 at 141 W/kg	7800 at 71.5 Wh/kg	4.2	68 % after 3000 cycles	[18]
Graphene-$Li_4Ti_5O_{12}$// Graphene/Sucrose	95 at 40 W/kg	3000 at 32 Wh/kg	3.0	87 % after 500 cycles	[19]
Li_3VO_4//AC	49.1 at 72.5 W/kg	129.7 at 24.5 Wh/kg	3.5	-	[20]
$LiTi_{1.5}Zr_{0.5}(PO_4)_3$// AC	46.7 at 79.2 W/kg	8120 at 9.91 Wh/kg	3.4	93 % after 100 cycles	[21]
Fe_3O_4-Graphene// 3D Graphene	147 at 150 W/kg	2587 at 86 Wh/kg	3.0	70 % after 1000 cycles	[22]
TiC//PHPNC[4]	112 at 450 W/kg	67500 at 35.6 Wh/kg	4.5	83%, 5000 cycles	[23]
Graphene-VN //carbon nanorods	162 at 200 W/kg	10000 at 64 Wh/kg	4.0	86%, 1000 cycles	[24]
CNT/V_2O_5//AC	25.5 at 40 W/kg	6300 at 6.9 Wh/kg	2.7	80%, 10000 cycles	[25]
TiO_2-B nanowire//CNT	12.5 at 300 W/kg	1300 at 8 Wh/kg	2.8	1000 cycles	[26]
TiP_2O_7//AC	13 at 46 W/kg	370 at 0.2 Wh/kg	3.0	78%, 500 cycles	[27]
Li-Hard carbon//AC	82 at 100 W/kg	50000 at 1 Wh/kg	2.8	100 % after 40 cycles	[28]

[1]FGO-functionalized graphene oxide, [2]AC-activated carbon, [3]FRGO-flash reduced graphene oxide, [4]PHPNC- pyridine-derived hierarchical porous nitrogen-doped carbon

References

[1] D. H. Sim, X. Rui, J. Chen, H. Tan, T. M. Lim, R. Yazami, H. H. Hng, Q. Yan, Direct growth of $FeVO_4$ nanosheet arrays on stainless steel foil as high-performance binder-free Li ion battery anode, *RSC Advances*, **2012**, 2, 3630-3633

[2] N. Yan, Y. Xu, H. Li, W. Chen, The preparation of $FeVO_4$ as a new sort of anode material for lithium ion batteries, *Mater. Lett.* **2016**, 165, 223-226

[3] X. Liu, Y. Cao, H. Zheng, X. Chen, C. Feng, Synthesis and modification of $FeVO_4$ as novel anode for lithium-ion batteries, *Appl. Surf. Sci.* **2017**, 394, 183-189

[4] H. Li, X. Liu, T. Zhai, D. Li, H. Zhou, Li_3VO_4: A Promising Insertion Anode Material for Lithium-Ion Batteries, *Adv. Energy Mater.* **2013**, *3*, 428-432

[5] S. Ni, J. Zhang, J. Ma, X. Yang, L. Zhang, Li_3VO_4/N-doped graphene with high capacity and excellent cycle stability as anode for lithium ion batteries, *J. Power Sources* **2015**, 296, 377-382

[6] L. Chen, X. Jiang, N. Wang, J. Yue, Y. Qian, J. Yang, Surface-Amorphous and Oxygen-Deficient $Li_3VO_{4-\delta}$ as a Promising Anode Material for Lithium-Ion Batteries, *Adv. Sci.* **2015**, *2*, 1500090

[7] L. L. Zhou, S. Y. Shen, X. Peng, L. N. Wu, Q. Wang, C. H. Shen, T. T. Tu, L. Huang, J. T. Li, S. G. Sun, New insights into the structure changes and interface properties of Li_3VO_4 anode for lithium ion batteries during the initial cycle by in-situ techniques, *ACS Appl. Mater. Interfaces*, **2016**, *8*, 23739-23745

[8] Y. Yang, J. Li, D. Chen, J. Zhao, Spray Drying-Assisted Synthesis of Li_3VO_4/C/CNTs Composites for High-Performance Lithium Ion Battery Anodes, *J. Electrochem. Soc.* **2017**, 164, A6001-A6006

[9] C. Zhang, C. Liu, X. Nan, H. Song, Y. Liu, C. Zhang, G. Cao, Hollow-cuboid Li_3VO_4/C as High Performance Anodes for Lithium-Ion Batteries, *ACS Appl. Mater. Interfaces*, **2016**, *8*, 680-688

[10] K. Wang, C. Zhang, H. Fu, C. Liu, Z. Lia, W. Ma, X. Lu, G. Cao, Enhanced electrochemical properties of Li_3VO_4 with controlled oxygen vacancies as Li-ion battery anode, *Chem. Eur. J.* **2017**, 10.1002/chem.201700150

[11] Q. Li, Q. Wei, J. Sheng, M. Yan, L. Zhou, W. Luo, R. Sun, L. Mai, Mesoporous Li_3VO_4/C Submicron-Ellipsoids Supported on Reduced Graphene Oxide as Practical Anode for High Power Lithium-Ion Batteries, *Adv. Sci.* **2015**, 1500284

[12] Z. Jian, M. Zheng, Y. Liang, X. Zhang, S. Gheytani, Y. Lan, Y. Shi, Y. Yao, Li_3VO_4 anchored graphene nanosheets for long-life and high-rate lithium-ion batteries, *Chem. Commun.*, **2015**, 51, 229-231

[13] C. Zhang, H. Song, C. Liu, Y. Liu, C. Zhang, X. Nan, G. Cao, Fast and Reversible Li Ion Insertion in Carbon-Encapsulated Li_3VO_4 as Anode for Lithium-Ion Battery, *Adv. Funct. Mater.* **2015**, 25, 3497–3504

[14] S. Ni, X. Lv, J. Ma, X. Yang, L. Zhang, Electrochemical characteristics of lithium vanadate, Li_3VO_4 as a new sort of anode material for Li-ion batteries, *J. Power Sources* **2014**, 248, 122-129

[15] Y. Yang, J. Li, X. He, J. Wang, D. Sun, J. Zhao, Facile spray drying route for mesoporous Li_3VO_4/C hollow spheres as an anode for long life lithium ion batteries, *J. Mater. Chem. A*, **2016**, 4, 7165-7168

[16] M. Y. Shad, M. Nouri, A. Salmasifar, H. Sameie, R. Salimi, H. Eivaz Mohammadloo, A. A. Sabbagh Alvani, M. Ashuri, M. Tahriri, Wet-Chemical Synthesis and Electrochemical Properties of Ce-Doped $FeVO_4$ for Use as New Anode Material in Li-ion Batteries, *J. Inorg. Organomet. Polym.* **2013**, 23, 1226

[17] Jain, A. et al., Activated carbons derived from coconut shells as high energy density cathode material for Li-ion capacitors, *Sci. Rep.* **3**, 3002 (2013)

[18] Zhang, T. et al., High energy density Li-ion capacitor assembled with all graphene-based electrodes, *Carbon* **92**, 106-118 (2015).

[19] Leng, K. et al., Graphene-based Li-ion hybrid supercapacitors with ultrahigh performance, *Nano Res.* **6**, 581-592 (2013).

[20] Wei, H. Y., Tsai, D. S., Hsieh, C. L., Prelithiated lithium vanadate anode and the mass balancing of its hybrid capacitor, *RSC Adv.*, **5**, 69176-69183 (2015)

[21] Peng, C. J., Tsai, D. S., Chang, C., Wei, H. Y., The lithium ion capacitor with a negative electrode of lithium titanium zirconium phosphate, *J. Power Sources* **274**, 15-21 (2015)

[22] Zhang, F. et al., A high-performance supercapacitor-battery hybrid energy storage device based on graphene-enhanced electrode materials with ultrahigh energy density, *Energy Environ. Sci.*, **6**, 1623-1632 (2013)

[23] Wang, H.; et al. A high-energy lithium-ion capacitor by integration of a 3D interconnected titanium carbide nanoparticle chain anode with a pyridine-derived porous nitrogen-doped carbon cathode, *Adv. Funct. Mater.***26**, 3082-3093 (2016)

[24] Wang, R., Lang, J., Zhang, P., Lin, Z., Yan, X., Fast and Large Lithium Storage in 3D Porous VN Nanowires–Graphene Composite as a Superior Anode Toward High-Performance Hybrid Supercapacitors, *Adv. Funct. Mater.* **25**, 2270-2278 (2015)

[25] Chen, Z. et al., High-Performance Supercapacitors Based on Intertwined CNT/V_2O_5 Nanowire Nanocomposites, *Adv. Mater.* **23**, 791-795 (2011)

[26] Wang, Q., Wen, Z., Li, J., A Hybrid Supercapacitor Fabricated with a Carbon Nanotube

Cathode and a TiO_2–B Nanowire Anode, *Adv. Funct. Mater*. **16**, 2141-2146 (2006)

[27] Aravindan, V. et al., Hybrid supercapacitor with nano-TiP_2O_7 as intercalation electrode, *J. Power Sources*, **196**, 8850-8854 (2011)

[28] Cao, W. J., Zheng, J. P., Li-ion capacitors with carbon cathode and hard carbon/stabilized lithium metal powder anode electrodes, *J. Power Sources* **213**, 180-185 (2012)